Acta Pharmaceutica Sinica B 2020;10(12):2384–2403

Chinese Pharmaceutical Association
Institute of Materia Medica, Chinese Academy of Medical Sciences

Acta Pharmaceutica Sinica B

www.elsevier.com/locate/apsb
www.sciencedirect.com

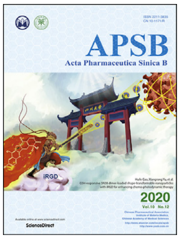

ORIGINAL ARTICLE

Bone-seeking nanoplatform co-delivering cisplatin and zoledronate for synergistic therapy of breast cancer bone metastasis and bone resorption

Yanjuan Huang, Zhanghong Xiao, Zilin Guan, Zishan Zeng, Yifeng Shen, Xiaoyu Xu, Chunshun Zhao*

School of Pharmaceutical Sciences, Sun Yat-sen University, Guangzhou 510006, China

Received 16 March 2020; received in revised form 8 June 2020; accepted 10 June 2020

KEY WORDS

Bone metastasis;
Bone targeting;
Osteolysis;
Zoledronate;
Cisplatin

Abstract The "vicious cycle" established between tumor growth and osteolysis aggravates the process of breast cancer bone metastasis, leading to life-threatening skeletal-related events that severely reduce survival and quality of life. To effectively interrupt the "vicious cycle", innovative therapeutic strategies that not only reduce osteolysis but also relieve tumor burden are urgently needed. Herein, a bone-seeking moiety, alendronate (ALN), functionalized coordination polymer nanoparticles (DZ@ALN) co-delivering cisplatin prodrug (DSP) and antiresorptive agent zoledronate (ZOL) *via* Zn^{2+} crosslinking for combination therapy was reported. The versatile DZ@ALN with a diameter of about 40 nm can cross the fissure in the bone marrow sinus capillaries, and possesses an excellent bone-seeking ability both *in vitro* and *in vivo*. Additionally, DZ@ALN could synergistically inhibit the proliferation of cancer cells, suppress the formation of osteoclast-like cells and induce the apoptosis of osteoclasts *in vitro*. Importantly, it could preferentially accumulate in bone affected site, remarkably inhibit the proliferation of tumor cells, relieving bone pain, and significantly inhibit the activation of osteoclasts, protecting the bone from destruction *in vivo*, eventually leading to the breakdown of "vicious cycle" without inducing obvious systemic toxicity. This innovative nanoagent combines chemotherapy and osteolysis inhibition, exhibiting an inspiring strategy for effective treatment of bone metastasis.

---

*Corresponding author. Tel./fax: +86 20 39943118.
E-mail address: zhaocs@mail.sysu.edu.cn (Chunshun Zhao).

Peer review under responsibility of Chinese Pharmaceutical Association and Institute of Materia Medica, Chinese Academy of Medical Sciences.

https://doi.org/10.1016/j.apsb.2020.06.006

1. Introduction

The most popular cancer, breast cancer, that affects women worldwide, has a great avidity for bone, and up to 65%−80% stage IV breast cancer patients can develop bone metastasis[1−3], where about 85% of patients are associated with predominantly osteolytic lesions[4]. Osteolytic bone metastases are often devastating and usually incurable, which cause pathological fractures, spinal cord compression, life-threatening hypercalcemia and severe unbearable pain[1,5], leading to significantly increased mortality rate and seriously reduced quality of life.

Bone microenvironment provides a fertile soil for tumor cells flourish. Once tumor cells metastasize to bone, it can overproduce cytokines to activate osteoclasts bone absorption, destroying the bone marrow microenvironment. In turn, osteolysis further stimulates the proliferation of tumor cells, aggravating the bone metastasis progress. In this way, a "vicious cycle" is established between the tumor cells and osteoclasts, which correlates tumor growth with osteolysis, leading to a poor prognosis of bone metastasis[6]. Thus, inhibition of tumor growth and osteolysis simultaneously in bone metastatic region is crucial to achieve efficient therapy against bone metastasis.

Antiresorptive drugs, bisphosphonates (BPs), have been widely employed to disrupt the "vicious cycle" by blocking the activity of osteoclasts for the prevention and treatment of bone metastasis in the past two decades, benefiting from their powerful osteoclasts inhibition and bone-seeking ability[7]. Zoledronic acid (ZOL), a representative third-generation BPs, has been reported to be the most potent antiresorptive agent among other BPs. ZOL can be rapidly distributed to bone with two phosphonate groups[8], especially the bone lesion site, and can be ingested by osteoclasts to effectively alleviate bone resorption by inhibiting its activity. Treatment with BPs, particularly ZOL, could lead to a remarkable decrease in the morbidity and the rate of bone loss involved with bone metastasis[9]. What's more, researches also showed that BPs, notably ZOL, could inhibit the invasion and proliferation of tumor cells in the marrow cavity, and the adhesion of tumor cells to the bone matrix[10]. Whereas, the use of ZOL alone does not effectively kill tumor cells, and high dosage of BPs can induce osteonecrosis in the jaw in clinic[11]. Thus it appears that though ZOL can slow down the process of osteolysis to some extent, unilateral inhibition of osteoclasts is not enough to entirely disturb the "vicious circle", failing to bring about healing.

Identically, despite that chemotherapy is the main approach to efficaciously suppress tumor cells, due to the low permeability and poor blood supply of bone tissue, high-dose and high-frequency chemotherapeutic agents are required to achieve effective therapeutic concentrations in bone metastatic site, resulting in severe side effects to healthy tissues. What's more, the single chemotherapy mechanism cannot effectively break the "vicious circle" as well, which can easily lead to drug resistance, tumor metastasis and recurrence. Because of the complicated crosstalk between the tumor cells and the bone microenvironment, combining two or more therapeutic agents that have multiple mechanisms of action to further interrupt the "vicious circle" on a multifaceted level is highly desired. Thus, combining ZOL with chemotherapeutic agents and concurrently deliver both agents to bone metastatic site can be an emerging strategy that not only can effectively inhibit both cancer cells and osteoclasts, but also can significantly lower doses of poorly selective chemotherapeutic agents, thereby reducing dose-related side effects.

Fortunately, platinum(II)-based chemotherapeutic agents, especially cisplatin (CDDP), have been widely used in the treatment of solid tumors by interfering with transcription and deoxyribonucleic acid (DNA)-mediated cellular functions[12−14]. However, due to their poor selectivity and severe side effects, much attention has recently been paid to the development of platinum(IV) prodrug-based nanoscale drug delivery systems. Platinum(IV) complexes can undergo intracellular reduction to produce active platinum(II) species and exhibit an increased stability and reduced side effects compared with platinum(II) complex[15,16]. Nanoparticles, including gold nanoparticles[17], MnO_2 nanosheets[18], polymeric micelles[19,20], Fe_3O_4 nanocarriers[21] and coordination polymer nanoparticles (CPNP)[22−24], have been reported to deliver CDDP prodrug *cis*,*cis*,*trans*-diamminedichlorodisuccinato-platinum (DSP) for enhanced cancer therapy. Among them, CPNP, a kind of emerging materials cross-linked by metal ions or clusters and organic linkers, possesses a great many of advantages, such as tunable sizes and compositions, high drug loadings, pH responsive drug release and intrinsic biodegradability[16], making it the most promising carrier.

Therefore, in this work, a bone-seeking ultrasmall coordination polymer nanoparticles (DZ@ALN) co-delivering chemotherapeutics DSP and antiresorptive agent ZOL to achieve the synchronous inhibition of tumor cells and osteoclasts was constructed. Alendronate (ALN), a bone-seeking moiety, was linked to fatty acid modified polyethylene glycols (PEG), to serve as bone-seeking material which coated on the surface of CPNP for preferential bone-targeting. The core of nanoparticles (DZ@DOPA) was prepared by crosslinking the carboxyl group of DSP and the bisphosphonate group of ZOL with Zn^{2+} using reverse microemulsion method, then it was further modified with outer lipid and the bone-seeking materials to form the final DZ@ALN (Scheme 1). The as-designed DZ@ALN with diameter about 40 nm could easily cross the fissure in the bone marrow sinus capillaries which is about 80−100 nm[25−27]. It co-delivers hydrophobic DSP and hydrophilic ZOL and releases platinum drugs and ZOL in a synchronized mode for synergistic inhibition of tumor cells and osteoclasts.

Moreover, the functionalization of bone-seeking materials can improve pharmacokinetics and selective bone-targeting. Compared with free drug combinations, DZ@ALN could normalize the pharmacokinetics and selective distribution of the co-delivered agents, thus endowing the ability to achieve optimal therapeutic effects with minimal toxicity. Results showed that DZ@ALN could precisely accumulate in the bone affected site, where the low pH triggered the rapid release of platinum drugs and ZOL in a synchronous mode, thereby synergistically

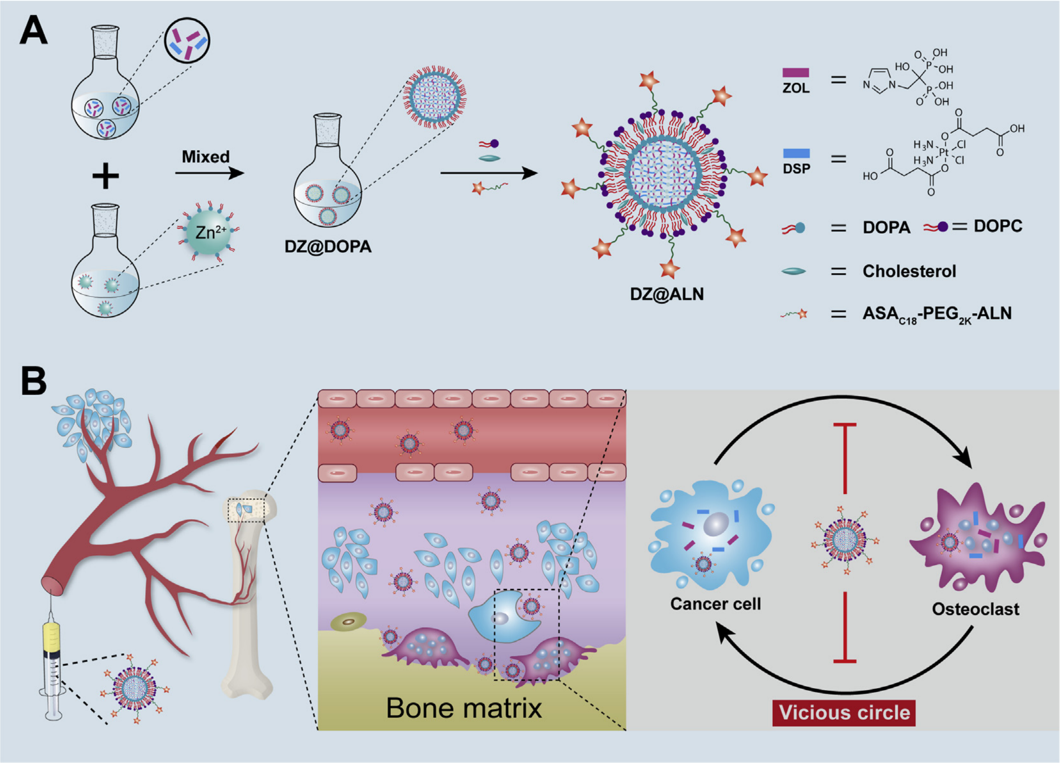

Scheme 1 (A) The preparation of ZOL and DSP loaded bone-targeting DZ@ALN nanoparticles. (B) Schematic illustration of bone-targeted delivery of DZ@ALN for synchronous inhibition of cancer cells and osteoclasts, eventually breakdown the "vicious cycle".

inhibiting the growth of tumor cells, and suppressing the activation and the function of osteoclasts simultaneously, destroying the "seed and soil" between tumor cells and osteoclasts to reduce tumor burden and osteolysis. This innovative nanoplatform that suppresses tumor growth and bone resorption simultaneously provides a new idea for the treatment of bone metastasis.

2. Materials and methods

2.1. Materials and cell lines

Cisplatin (CDDP, 99.99%), zoledronate (ZOL, ≥98%), 1,1′-dioctadecyl-3,3,3′,3′-tetramethylindocarbocyanine perchlorate (DiI, ≥98%) and 1,1′-dioctadecyl-3,3,3′,3′-tetramethyl indotricarbocyanine Iodide (DiR, ≥95%) were purchased from Aladdin Industrial Co. (Shanghai, China). Hydroxyapatite (HA), acid phosphatase, leukocyte (TRAP) kit, 3-(4,5-dimethyl-2-thiazolyl)-2,5-diphenyl-2-*H*-tetrazolium bromide (MTT) and penicillin−streptomycin were purchased from Sigma−Aldrich (St. Louis, MO, USA). Fetal bovine serum (FBS), pancreatic enzymes and Dulbecco's modified Eagle's medium (DMEM) were purchased from Gibco (Grand Island, NY, USA). Recombinant murine sRANK ligand (RANKL) was purchased from PeproTech (Rocky Hill, NJ, USA). 1,2-Dioleoyl-*sn*-glycero-3-phosphocholine (DOPC), dioleoylphosphatidic acid (DOPA) and cholesterol were purchased from Avanti Polar Lipids, Inc. (Alabaster, AL, USA). Dialysis membrane (molecular weight cutoff: 3500 Da, Sangon Biotech, Shanghai, China). Ultrapure water (18.2 Ω) was acquired from an Ultra Bio Mk2 ultrapure system (Elga, High Wycombe, UK). Annexin V/PI Apoptosis Detection Kit was obtained from MultiSciences (Hangzhou, China). Chemicals and solvents were used directly without further purification.

MDA-MB-231 cells, 4T1 cells and murine osteoclasts precursor RAW 264.7 cells were purchased from the Laboratory Animal Center of Sun Yat-sen University, Guangzhou, China. The three cells were cultured in DMEM supplemented with 10% FBS, 1% penicillin−streptomycin at 37 °C in a humidified incubator containing 5% CO_2.

2.2. Synthesis and characterization of DZ@ALN nanoparticles

DSP, bone-targeting ASA_{C18}-PEG_{2k}-ALN and non-targeting ASA_{C18}-PEG_{2k} materials were synthesized according to our reported method[24,28]. DOPA-coated nanoparticles, DZ@DOPA, were obtained by the microemulsion method[29−31]. Briefly, 0.2 mL of a mixed sodium salt solution of DSP (15 mg/mL) and ZOL (with molar ratio DSP/ZOL = 2:1, 1:1 and 1:2) was added into 5 mL oil phase (0.3 mol/L Triton X-100 and 1.5 mol/L 1-hexanol in cyclohexane) with vigorously stirring for 10 min at room temperature to form a water-in-oil (W/O) emulsion. Two hundred microliters of $ZnCl_2$ (12.5 mg/mL) aqueous solution was added into another 5 mL of the above oil phase and stirred in a similar manner to form the other similar W/O emulsion. Twenty microliters of 100 mg/mL DOPA (Avanti Polar Lipids, Inc.) solution was added into the W/O emulsion containing Zn^{2+} under stirring. Then the W/O emulsion containing drug was slowly added into the Zn^{2+} solution and kept stirring for an additional 30 min. By adding 10 mL ethanol, DZ(2:1)@DOPA, DZ(1:1)@DOPA and DZ(1:2)@DOPA nanoparticles which carrying different drug ratios of DSP and ZOL respectively were obtained, and then centrifuged at 17,745×*g* (GL-20C, Anting, Shanghai, China) for

15 min, washed twice with ethanol/THF (1:1) and once with ethanol, then redispersed in $CHCl_3$ and stored at 4 °C for further use. DSP@DOPA and ZOL@DOPA which carrying DSP or ZOL for monotherapy were synthesized similar to that of DZ@DOPA nanoparticles.

The final DZ@ALN was prepared by the addition of a $CHCl_3$ solution of ASA_{C18}-PEG_{2k}-ALN and DOPC/cholesterol (2:1 molar ratio) (Avanti Polar Lipids, Inc.) to DZ@DOPA, blending, then the $CHCl_3$ was completely evaporated, followed by re-dispersed in PBS with ultrasound, then centrifuged at high-speed for purification, and further resuspended in PBS or DMEM. Single drug loaded DSP@ALN and ZOL@ALN were prepared by the similar method. In addition, DZ@PEG was prepared by replacing ASA_{C18}-PEG_{2k}-ALN with ASA_{C18}-PEG_{2k} using an identical method.

The hydrodynamic diameters and zeta potentials of nanoparticles were determined by dynamic light scattering (DLS) using a Malvern Zetasizer Nano ZS 90 (Malvern Instruments, Malvern Ltd., Worcestershire, UK). The morphology of the nanoparticles was observed by transmission electron microscopy (TEM, JEM-1400, JEOL, Tokyo, Japan). The nanoparticles were dried and weighed for drug content measurement. To determine the platinum drug loading, the samples were digested in aqua regia overnight, dried and dissolved with 1% HNO_3. The platinum (Pt) content in the nanoparticles was calculated by comparing the absorbance with a standard curve of K_2PtCl_4 using Graphite Furnace Atomic Absorption Spectrometer (GFAAS, AAnalyst 800, Perkin−Elmer, Norwalk, CT, USA). ZOL loading was detected by UV−Vis spectroscopy (Techcomp, UV2600 spectrophotometer, Shanghai, China). Briefly, the dried nanoparticles were digested with 0.4 mol/L HCl overnight at room temperature. The content of ZOL was obtained by comparing the absorbance at 215 nm with a standard curve of ZOL established in 0.4 mol/L HCl[32]. For the drug loading of DZ@ALN, using the platinum loading from GFAAS and corresponding to the standard curve of DSP, the absorbance of platinum was subtracted from the total absorbance to calculate the drug loading of ZOL. The interactions between drugs, Zn^{2+} and DOPA were investigated using Fourier transform infrared spectroscopy (FTIR, VERTEX 70, Bruker, Germany). The atomic composition of DZ(1:1)@DOPA on the surface was characterized by X-ray photoelectron spectroscopy (XPS, ESCALAB 250, Thermo Fisher Scientific, Asheville, NC, USA).

2.3. *In vitro stability and drug release studies*

The *in vitro* stability of DZ(1:1)@ALN was investigated by monitoring the particle size changes in water, PBS, and DMEM containing 10% FBS for one week using DLS (Malvern Instruments Ltd., Worcestershire, UK) and TEM (JEM-1400).

In vitro drug release profiles were determined in 50 mL PBS buffer at different pH values using dialysis method. A suspension of 1 mL DZ(1:1)@ALN or ZOL@ALN with known platinum and Zn^{2+} amount were placed in a dialysis bag, and then immersed in PBS buffer. The dialysis was kept in a shaker under stirring at 100 rpm (ZHWY-200D shaker, Zhicheng Co., Shanghai, China). At specified time schedules, 10 mL sample was withdrawn from the dissolve medium and fresh medium at an equal volume was immediately replenished. The amount of released platinum and Zn^{2+} were detected by GFAAS (Perkin−Elmer) and Inductively Coupled Plasma-Atomic Emission Spectroscopy (ICP-AES, Optima 8300, Perkin−Elmer, Waltham, MA, USA), respectively. All the results were calculated using Eq. (1):

$$\text{Release}\ (\%) = \frac{C_{\text{sample}\ (n)} \times 50}{C_{\text{NP}} \times 1} \times 100 + \frac{\sum_{i=1}^{n-1} \left[\left(C_{\text{sample}\ (n-1)} \times 50 \right) / \left(C_{\text{NP}} \times 1 \right) \right] \times 10}{50} \tag{1}$$

where $C_{\text{sample}(n)}$ represents the platinum or Zn^{2+} concentration in the samples determined by GFAAS or ICP-AES at specified time points. C_{NP} represents the initial platinum or Zn^{2+} concentration in the nanoparticles.

2.4. *In vitro bone affinity studies*

The affinity to HA and bone fragments were investigated to evaluate the *in vitro* bone targeting ability of DZ(1:1)@PEG and DZ(1:1)@ALN. Briefly, DiI-labled DZ(1:1)@PEG and DZ(1:1)@ALN were suspended in 3 mL PBS (pH 7.4) in centrifuge tubes at an equivalent DiI (Aladdin Industrial Co.) concentration (2.5 μmol/L). Then 50 mg HA (Aladdin Industrial Co.) power was added and gently shaken at 50 rpm (ZHWY-200D shaker, Zhicheng Co., Chengdu, China) for 30 min, 1, 2 and 4 h at room temperature, respectively. In the meantime, the nanoparticles without HA incubation were served as control. At predetermined time intervals, the mixtures were centrifuged at 1400×*g* (L500, Cence, Changsha, China) for 5 min and the concentrations (*C*) of DiI in the supernatants were measured by fluorescence spectrometer (Fluoromax-4, HORIBA, Piscataway, NJ, USA; λ_{ex} = 500 nm, λ_{em} = 560 nm). The HA binding (%) was determined using Eq. (2):

$$\text{HA binding}\ (\%) = \left[\left(C_{\text{without HA}} - C_{\text{with HA}} \right) / \left(C_{\text{without HA}} \right) \right] \times 100 \tag{2}$$

where $C_{\text{with HA}}$ and $C_{\text{without HA}}$ represent the concentration of DiI with or without HA incubation, respectively.

The affinity of DiI-labled DZ(1:1)@PEG and DZ(1:1)@ALN to skull fragments which obtained from fetal rats were investigated. Briefly, the periostea of the harvested skulls were removed under a stereoscopic microscope[33] before drying in an oven. Free DiI, DiI-labled DZ(1:1)@PEG and DZ(1:1)@ALN were incubated with the skull fragments for 30 min, 1, 2 and 4 h at 100 rpm (ZHWY-200D shaker, Zhicheng Co.). After washing and drying under dark, the binding capacity of different groups was evaluated by imaging under an inverted fluorescent microscope (IX73, Olympus, Tokyo, Japan).

2.5. *Cytotoxicity assays and synergistic effects of drug combinations*

In vitro cytotoxicity assays were performed on MDA-MB-231, 4T1 and RAW 264.7 cell lines. The cells were trypsinized and counted, and then seeded into 96-well plate (4 × 10^3 cells/well), followed by further incubating for 24 h. The culture media was replaced by 100 μL of fresh medium containing different concentration of various drug formulations, and the cells were treated for 72 h. Cell viability was measured using MTT method. The optical density was measured using a microplate reader (ELX800, Bio-Tek, Doraville, GA, USA) at a wavelength of 490 nm. The combination index (CI) was calculated using Eq. (3) [34,35]:

$$\mathrm{CI} = \frac{D_1}{D_{\mathrm{m1}}} + \frac{D_2}{D_{\mathrm{m2}}} \tag{3}$$

where D_1 and D_2 are the doses of drug 1 and drug 2 in combination that produce a specific drug effect (*e.g.*, 50% inhibitory concentration), while D_{m1} and D_{m2} are drug concentrations at which the same drug effect achieved when dosed individually. Usually, the CI values are plotted against drug effect levels (IC_x values), and CI values lower than, equal to, and greater than 1 denote synergism, additivity, and antagonism, respectively.

2.6. *In vitro osteoclastogenesis*

RAW 264.7 cells are a widely used pre-osteoclast model[36], it can differentiate into osteoclasts when stimulated with RANKL[36−38]. Briefly, RAW 264.7 cells were seeded on glass coverslips in 24-well plates (5×10^3 cells/well) and incubated for 24 h. The culture medium was replaced by fresh medium containing 50 ng/mL RANKL (PeproTech). The media was replaced every 2 days. At Day 4, The culture media was replaced by 500 μL fresh medium containing 50 ng/mL RANKL and certain amount of free CDDP, free ZOL, DSP@ALN, ZOL@ALN and DZ(1:1)@ALN, and cells were treated for another 48 h. The cells not exposed to drug treatment but treated with or without RANKL were served as control. At Day 6, the cells were stained with TRAP Kit (Sigma−Aldrich) according to the manufacturer's instructions to evaluate the formation of osteoclasts (multinucleated cells $\geq$3 nuclei).

2.7. *In vitro cell apoptosis*

Apoptosis analysis was performed with Annexin V/PI Apoptosis Detection Kit (MultiSciences). Briefly, MDA-MB-231, RAW 264.7 cells and osteoclasts were seeded in 6-well plates (2×10^5 cells), after 24 h incubation, the cells were treated with different drug formulations for 48 h. Cells incubated with fresh culture media were served as control. The floating and adherent cells were harvested and doubly stained with Annexin V-FITC and PI based on the manufacturer's instructions, and then analyzed by flow cytometer (FCM, Guava EasyCyte 6-2L, Merck Millpore, Hayward, CA, USA).

2.8. *Animals and animal model of bone metastasis*

Male Sprague−Dawley rats (SD, 180−200 g), female BALB/c-*nu*/*nu* mice (20 ± 2 g, 6 weeks old) and female Kunming mice (20 ± 2 g) were purchased from the Laboratory Animal Center of Sun Yat-sen University, Guangzhou, China. All experimental procedures were approved and supervised by the Institutional Animal Care and Use Committee of Sun Yat-sen University. Intratibia injection method was used to establish the BALB/c-*nu*/*nu* mouse model of breast cancer bone metastasis. Typically, before injection, the mouse was anesthetized, and the tibia of the right hindlimb was carefully exposed. Then a needle (26-gauge) was used for the intra-tibia injection of MDA-MB-231 cells (6×10^5 cells) to prepare bone tumor models. The left tibia that only injected with PBS was served as control.

2.9. *In vivo pharmacokinetics and biodistribution studies*

2.9.1. *In vivo pharmacokinetics studies*

Briefly, CDDP, DZ(1:1)@PEG and DZ(1:1)@ALN were intravenously injected into SD rats (180 ± 20 g, $n = 3$) at an equivalent CDDP dose at 2 mg/kg. At different time schedules, blood samples were harvested and then centrifuged (1000×*g*, 10 min; Centrifuge 5427R, Eppendorf, Hamburg, Germany) to obtain plasma. The plasma (200 μL) was withdrawn and digested with 1 mL aqua regia overnight, then dried and the residue was redissolved in 1% $\mathrm{HNO_3}$ and then detected by GFAAS (Perkin−Elmer).

2.9.2. *In vivo biodistribution by fluorescence imaging and platinum detection*

For fluorescence imaging studies, free DiR (Aladdin Industrial Co.), DiR-labeled DZ(1:1)@PEG and DZ(1:1)@ALN were intravenously injected into the mice bearing bone metastatic tumors (0.25 mg/kg on DiR basis, $n = 3$). At selected time points of 2, 4, 8, 12, and 24 h, mice were anesthetized and captured *via* a small animal live imaging system (IVIS Lumina XRMS Series III, Perkin−Elmer, Waltham, MA, USA, excitation: 740 nm, emission: 790 nm). At 24 h post injection, mice were sacrificed and the hearts, livers, spleens, lungs, kidneys, left hindlimbs (healthy hindlimbs) and right hindlimbs (metastatic hindlimbs) were excised and imaged.

To detect the drug concentration in tissues, platinum was selected as a model drug to represent the distribution behavior of nanoparticles. Briefly, free CDDP, DZ(1:1)@PEG and DZ(1:1)@ALN were intravenously injected into the tumor-bearing mice (2 mg/kg on CDDP basis, $n = 3$ at each time points). At predetermined time points, mice were sacrificed and the hearts, livers, spleens, lungs, kidneys, left hindlimbs and right hindlimbs were excised, weighed and then digested overnight with aqua regia, dried and redissolved in 1% $\mathrm{HNO_3}$ before detected by GFAAS (Perkin−Elmer).

2.10. *In vivo therapeutic effect*

Tumor bearing BALB/c-*nu*/*nu* mice were randomly assigned into seven groups ($n = 6$). Each group was intravenously injected with one of the following formulations: PBS, free CDDP+ZOL, DSP@ALN, ZOL@ALN, DZ(1:1)@PEG, DSP@ALN+ZOL@ALN and DZ(1:1)@ALN at a dose of 0.25 mg/kg CDDP and 1 mg/kg ZOL. Injections were given every six days for a total of three injections. Animal body weight was recorded and tumor size was measured *via* vernier calipers every other day. The tumor volume (mm^3) was calculated based on Eq. (4):

$$\mathrm{Volume}\left(\mathrm{mm}^3\right) = (\mathrm{Tumor\ length}) \times (\mathrm{Tumor\ width})^2 \Big/ 2 \tag{4}$$

The pain-related behaviors were tested every other day as well. After a 5-min acclimation period, the spontaneous lifting time and the number of flinches were measured over a 4-min observation period according to the reported paper[39].

At the end of experiment, mice were sacrificed, bone metastatic hindlimbs were excised, fixed in 4% paraformaldedyde solution, and detected using a Biograph 3D micro-CT device (ZKKS-MCT-Sharp-I, Caskaisheng, Guangzhou, China). After scanning, the 3D images were reconstructed and morphometric parameters, such as BV/TV [the ratio between bone volume (BV) and tissue volume (TV)], trabecular numbers (Tb. N), and bone surface/bone volume ratio (BS/TV) were determined automatically using the ZKKS-MicroCT 4.1 analysis software. For histopathological analyses, bone tissues were decalcified in 10% EDTA for 3 weeks[40]. Both tumors and bone tissues were embedded in paraffin, cut to a thickness of 3 μm, then the tumors were stained with hematoxylin and eosin (H&E) and Ki67, and the bone tissues were stained with H&E and TRAP for tumor burden in the tibiae and osteoclasts analysis, respectively.

2.11. *Safety evaluation*

For blood biochemical analysis, two batch of mice were used, one for single-dose toxicity and another for multiple-dose toxicity. Briefly, Kunming mice were randomly divided into three groups ($n = 6$), mice were injected with saline, free CDDP + ZOL and DZ(1:1)@ALN (0.25 mg/kg of CDDP and 1 mg/kg ZOL) on Day 1 (single dose) and Days 1 and 6 (multiple dose). On Days 2 and 7, blood samples were collected by enucleation manner without anticoagulant. The samples were centrifuged at 4 °C (1000×g, 15 min, Eppendorf) and serum was collected. Aspartate aminotransferase (AST) and alanine aminotransferase (ALT) were detected as indicators of liver function. Creatinine (CREA) and blood urea nitrogen (BUN) were determined as indicators of nephrotoxicity. The above blood biochemical indicators were detected by Automatic Analyzer (3100, Hitachi, Shanghai, China) according to the manufacture's instruction. In addition, major organs, including hearts, livers, spleens, lungs and kidneys, were harvested on Day 7 and fixed in 4% paraformaldedyde for more than 48 h. The samples were embedded into paraffin, sliced into approximately 3-μm thickness, and then stained with H&E before observed under an optical microscope (DM5000B, Leica, Wetzlar, Germany).

2.12. *Statistical analysis*

Results were presented as mean±standard deviation (SD). Multiple group comparisons of the means were performed by one-way analysis of variance (ANOVA). Social Sciences version 13.0 (SPSS 13.0, SPSS Inc., Chicago, IL, USA) statistical software was used to conduct all statistical analyses. The differences were considered significant for $^*P < 0.05$ and very significant for $^{**}P < 0.01$ or $^{***}P < 0.001$.

3. Results and discussions

3.1. *Synthesis and characterization of nanoparticles*

DZ@ALN was prepared *via* a two-step method (Scheme 1). The DOPA-capped nanoparticles (DZ@DOPA) were prepared by W/O microemulsion method. The Zn^{2+} ions crosslinking the carboxyl group of DSP and the bisphosphonate group of ZOL to form the core of nanoparticles *via* the formation of coordination bonds, and DOPA was served as a surfactant to stabilize the resulting DZ@DOPA *via* Zn-phosphate interactions simultaneously. By adjusting the reaction molar ratio of DSP and ZOL from 2:1 to 1:2, DOPA coated nanoparticles with different drug combinations, including DZ(2:1)@DOPA, DZ(1:1)@DOPA and DZ(1:2)@DOPA, were successfully synthesized. DSP@DOPA and ZOL@DOPA were similarly prepared by adding single drug DSP or ZOL, respectively.

The coordination structure of DOPA-coated nanoparticles was characterized by FTIR. The FTIR spectra of various nanoparticles are shown in Fig. 1A and Supporting Information Figs. S1A and S1B. For ZOL, peaks at 1546 and 1577 cm^{-1}, and bands at 1404 and 1453 cm^{-1} are attributed to the vibrations of CH═CH and C−N bonds, the stretching vibrations of C−H bonds in imidazole ring, respectively. DSP shows a characteristic $-NH_3$ stretching band at 3246 cm^{-1} and a very strong C═O stretching band at 1705 and 1663 cm^{-1}.

ZOL@DOPA displayed peaks at 1546 and 1577 cm^{-1}, bands at 1404 and 1453 cm^{-1}, which are attributed to the characteristic peaks in imidazole ring. DOPA shows characteristic $-CH_2$ stretching bands at 2922 and 2855 cm^{-1}. Deprotonation of phosphate groups in ZOL and DOPA by Zn^{2+}, resulting in the blue shifts of P═O and P−O−C peaks to 1078 and 992 cm^{-1}, respectively[32]. DSP@DOPA and DSP-Zn show a blue shift of C═O from 1663 and 1705 to 1558 cm^{-1}, revealing that the carboxylate groups of DSP were coordinated with Zn^{2+}. Besides, a blue shift of the characteristic peaks of DOPA from 1070 to 992 cm^{-1} (P−O−C), 1178 to 1078 cm^{-1} (P═O) and 1740 to 1630 cm^{-1} (C═O) are observed, respectively, indicating that a coordination interaction between DOPA and Zn^{2+} occurred to enable the functionalization of DOPA on the surface. In a similar way, for DZ@DOPA, taking DZ(1:1)@DOPA for example, characteristic stretching bands at 2922 and 2855 cm^{-1} are ascribed to the $-CH_2$ group in DOPA. Peaks at 1546 and 1577 cm^{-1}, bands at 1404 and 1453 cm^{-1} are the characteristic peaks of imidazole ring. And characteristic P═O and P−O−C stretching bands at 1078 and 992 cm^{-1}, respectively, are attributed to the deprotonation of phosphate groups of DOPA and ZOL by Zn^{2+}. Broad peaks from 1701 to 1534 cm^{-1} may attribute to the blue shift of C═O peak of DSP and the characteristic peaks of ZOL. Similar results are shown in DZ(2:1)@DOPA and DZ(1:2)@DOPA. The FTIR results suggest that the DOPA coated nanoparticles were successfully synthesized.

Comparing the FTIR spectra of DSP-Zn, DZ(2:1,1:1,1:2)-Zn and ZOL-Zn, with the reaction molar ratio of DSP/ZOL decreases from 2:1, 1:1 to 1:2, the characteristic absorption peaks of nanoparticles at 1700−1400 cm^{-1} are getting closer to the single drug ZOL-Zn nanoparticles, indicating that the ZOL content in the nanoparticles increases with the increase of ZOL reaction content, confirming the successful preparation of dual-drug nanoparticles with different ratios of DSP and ZOL.

To further confirm the successful preparation of DOPA coated nanoparticles, the atomic composition of the representative nanoparticles DZ(1:1)@DOPA on the surface was analyzed using XPS. XPS results reveal that the surface of DZ(1:1)@DOPA contained 2.08% (mol/mol), 6.85% (mol/mol) and 0.24% (mol/mol) of N, P and Pt atoms, respectively (Fig. 1B and C). The high surface P/N molar ratio of 3.28 confirmed that nitrogen-free DOPA was coated on the surface of nanoparticles. The strong N 1s band and P 2p band could be ascribed to the N atom in imidazole and DSP, and P atoms in ZOL and DOPA, respectively. And the strong Pt 4f band could be attributed to the Pt atom in DSP. XPS results reveal that DSP and ZOL have been constructed in the core of DZ(1:1)@DOPA successfully. Field-Emission-SEM (Gemini500, Zeiss/Bruker, Karlsruhe, Germany) further confirms that DZ(1:1)@DOPA containing Zn, P and Pt atoms, indicating the successful synthesis of DZ(1:1)@DOPA (Fig. 1F).

The final ALN functionalized nanoparticles were obtained by further coating DOPC, cholesterol and ASA_{C18}-PEG_{2K}-ALN on the surface of DOPA-capped nanoparticles *via* hydrophobic/hydrophobic interactions. The drug loading content of the final bone-seeking nanoparticles are shown in Supporting Information Table S1, the molar ratio of Pt/ZOL of DZ(2:1)@ALN, DZ(1:1)@ALN and DZ(1:1)@ALN are 1:2, 1:4 and 1:8, respectively, further confirming the successful preparation of dual-drug nanoparticles. TEM images of ALN-functionalized nanoparticles show well-

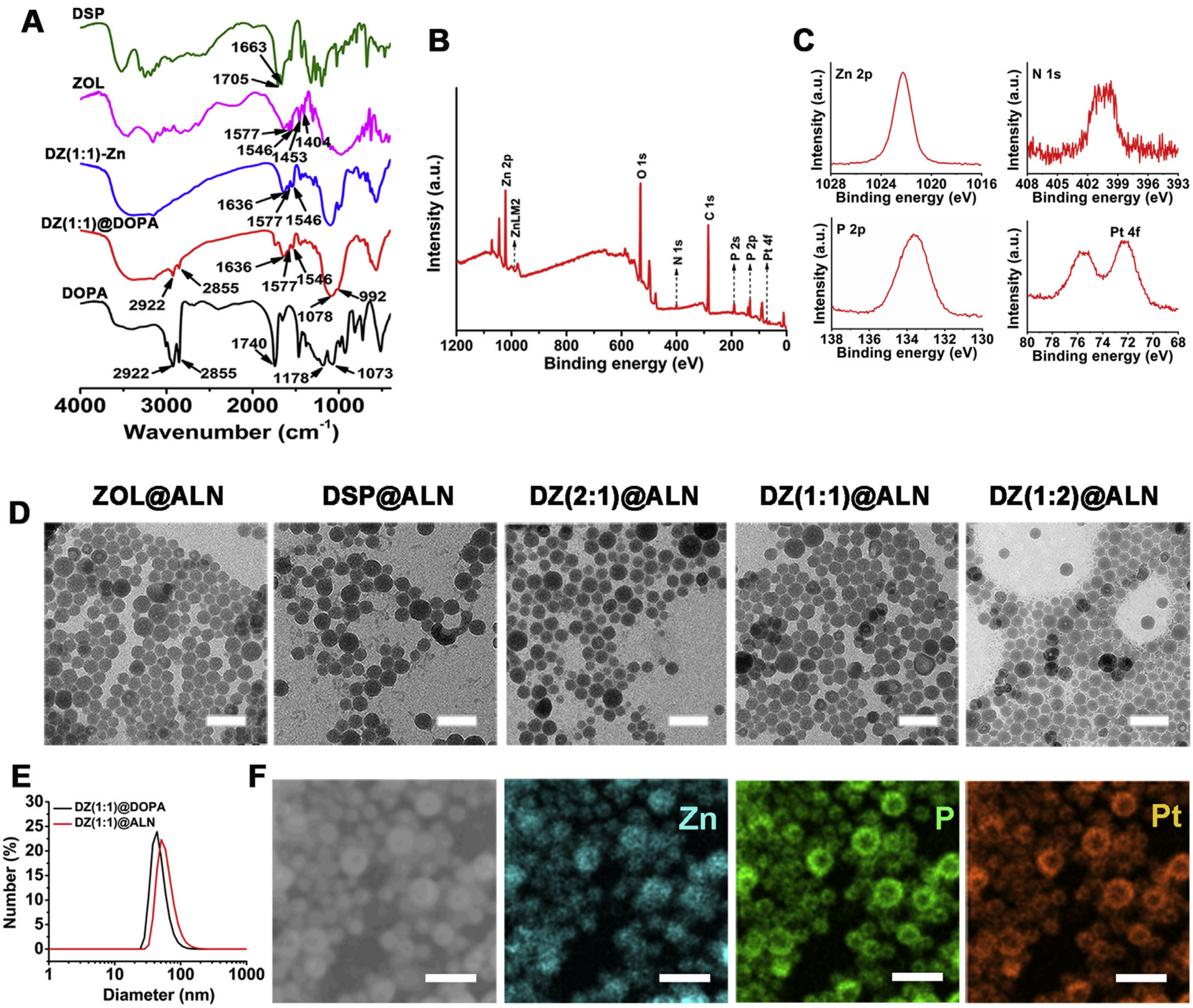

Figure 1 (A) FTIR spectra recorded for DSP, ZOL, DZ(1:1)-Zn, DZ(1:1)@DOPA and DOPA. (B) XPS survey spectrum recorded for DZ(1:1)@DOPA. (C) The Pt 4f, N 1s, P 2s and P 2p core-line spectrum recorded for the DZ(1:1)@DOPA. (D) TEM images of ZOL@ALN, DSP@ALN, DZ(2:1)@ALN, DZ(1:1)@ALN and DZ(1:2)@ALN without negative stain, scale bar: 100 nm. (E) Number-average diameter distributions of DZ(1:1)@DOPA and DZ(1:1)@ALN. (F) SEM image and SEM-EDS elemental mapping of DZ(1:1)@DOPA, scale bar: 100 nm.

Table 1 Average sizes and zeta potential of DOPA coated and final CPNP.

Reaction drug	Core of CPNP	Number-ave diameter (nm)	Final CPNP	Number-ave diameter (nm)	Zeta potential (mV)
ZOL	ZOL@DOPA	48.35 ± 2.71	ZOL@ALN	65.56 ± 1.92	−23.0 ± 0.93
DSP	DSP@DOPA	48.98 ± 2.12	DSP@ALN	63.50 ± 1.80	−23.7 ± 1.12
DSP&ZOL(2:1)	DZ(2:1)@DOPA	46.34 ± 1.92	DZ(2:1)@ALN	60.49 ± 4.41	−21.7 ± 0.15
DSP&ZOL(1:1)	DZ(1:1)@DOPA	47.87 ± 1.56	DZ(1:1)@ALN	61.00 ± 0.78	−23.5 ± 0.41
DSP&ZOL(1:2)	DZ(1:2)@DOPA	45.3 ± 1.10	DZ(1:2)@ALN	62.82 ± 4.52	−22.8 ± 0.65

Data were presented as mean ± SD (n = 3).

dispersed, uniform spheres with similar diameter at about 40 nm (Fig. 1D). The average size of the DOPA coated and the final nanoparticles measured by DLS are around 45 and 60 nm (Fig. 1E and Table 1), respectively. The relatively larger size of the ALN functionalized nanoparticles than the DOPA coated by DLS measurement might be ascribed to the coating of outer lipid. The superior particle size of less than 80 nm laded a foundation for excellent *in vivo* application.

The zeta potential (mV) of ASA_{C18}-PEG_{2K} coated nanoparticles is nearly neutral, while ASA_{C18}-PEG_{2K}-ALN functionalized nanoparticles display negative zeta potential at about −22 mV, possibly due to the polar diphosphate group of ALN, which indicated the successful functionalization of bone-seeking materials (Table 1 and Fig. S1C).

3.2. *In vitro stability and drug release studies*

The long-term stability of DZ(1:1)@ALN was investigated in water, PBS and DMEM containing 10% FBS for one week, and particle size changes were monitored by DLS and TEM, respectively. Negligible size changes were detected by DLS in the above three medium after one week incubation (Supporting Information Fig. S2A). Meanwhile, the particle size of DZ(1:1)@ALN maintained at around 40 nm, and the morphology was unchanged (Fig. S2B). These results indicted the excellent colloidal stability of DZ(1:1)@ALN.

The drug release profile of DZ(1:1)@ALN and ZOL@ALN were investigated under the mimicked various physiological conditions (pH 7.4, 6.5 and 5.0) at 37 °C. DZ(1:1)@ALN and ZOL@ALN exhibited strong pH-responsive drug release behavior (Fig. 2A, C and D). For ZOL@ALN, insignificant release behavior was observed under physiological condition of pH 7.4, with less than 10% was released within 8 h. However, the release rate increased significantly as pH decreased to 5, with more than 75% was released within 12 h. This was attributed to the dissociation of phosphate groups from Zn^{2+} through the protonation process of bisphosphonate group in ZOL ($pK_{a1} = 5.9$)[41] at acidic environment, weakening the coordination between Zn^{2+} and bisphosphonate group of ZOL. Since ZOL@ALN was composed by crosslinking Zn^{2+} and ZOL, the protonation and dissociation process could lead to the decomposition of the nanoparticles, resulting in the synchronous release of Zn^{2+} and ZOL. Thus the cumulative release rate of Zn^{2+} was detected.

Similarly, for DZ(1:1)@ALN, the release of platinum and Zn^{2+} were determined simultaneously to investigate the drug release behavior. Under physiological conditions, a little amount of drugs was released within 24 h, with 18% and 13% for platinum and Zn^{2+} respectively. When pH decreased to 6.5 and 5.0, a significant amount of drugs was released, with 56% and 63% at pH 5.0 within 8 h for platinum and Zn^{2+}, respectively. The rapid release of platinum at pH 5.0 from DZ(1:1)@ALN was possibly caused by the fracture of coordination bond at low pH values, as proved by many other research groups and our research teams[24,28,32,33]. In the bone metastatic microenvironment, the resorption of osteoclasts could lead to the secrete of hydrogen ions, keeping the pH to as low as 4.5−4.7[42,43]. Therefore, the constructed nanoparticles could remain relatively stable in blood circulation, but achieve rapid drug release once reaching the target site to improve the therapeutic effect.

3.3. *In vitro bone targeting studies*

As is well known that HA is abundant in bone microenvironment, especially in the bone metastatic site[44]. ALN has a great avidity for HA through the interaction between Ca^{2+} and the diphosphonate group. DZ(1:1)@PEG displayed non-specific binding capacity to HA during different incubation times, with HA binding (%) lower than 4% for up to 4 h incubation (Fig. 2B). In contrast, DZ(1:1)@ALN exhibited immediate binding to HA, with HA binding (%) reach up to 14.35% at 30 min, and with the incubation time increased to 4 h, HA binding (%) increased to 43.33%, suggesting the excellent binding ability than that of non-targeted DZ(1:1)@PEG.

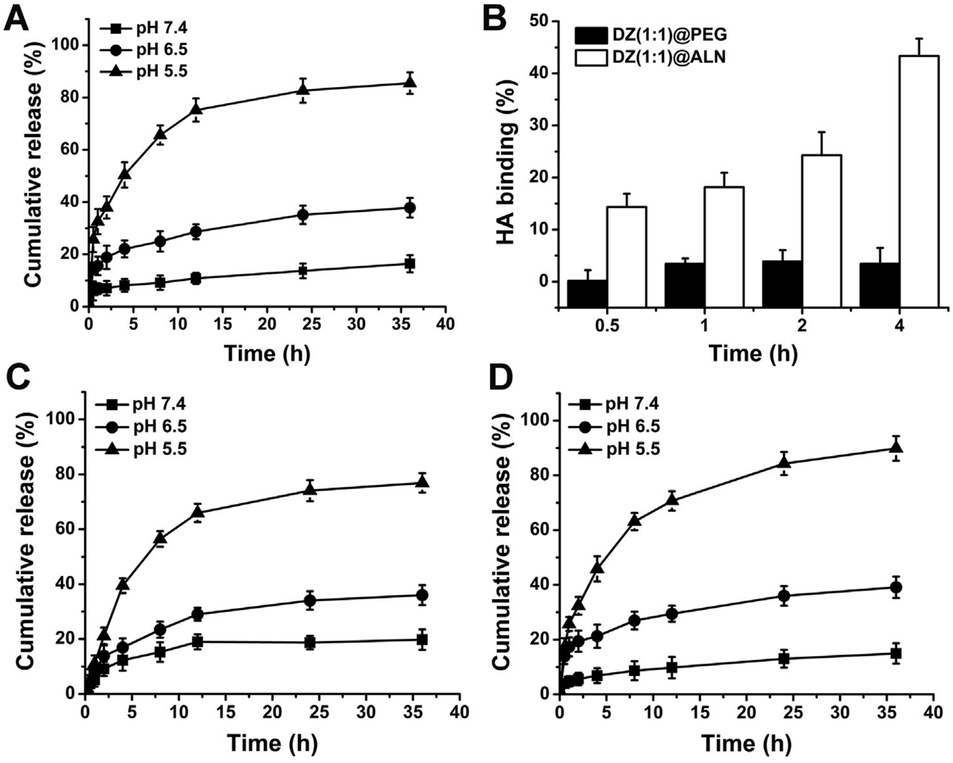

Figure 2 (A) Zn release behavior of ZOL@ALN at under 37 °C. (B) HA binding (%) of DZ(1:1)@PEG and DZ(1:1)@ALN. (C) *In vitro* platinum and (D) Zn release behaviors of DZ(1:1)@ALN at different pH conditions under 37 °C. Data are expressed as mean ± SD ($n = 3$).

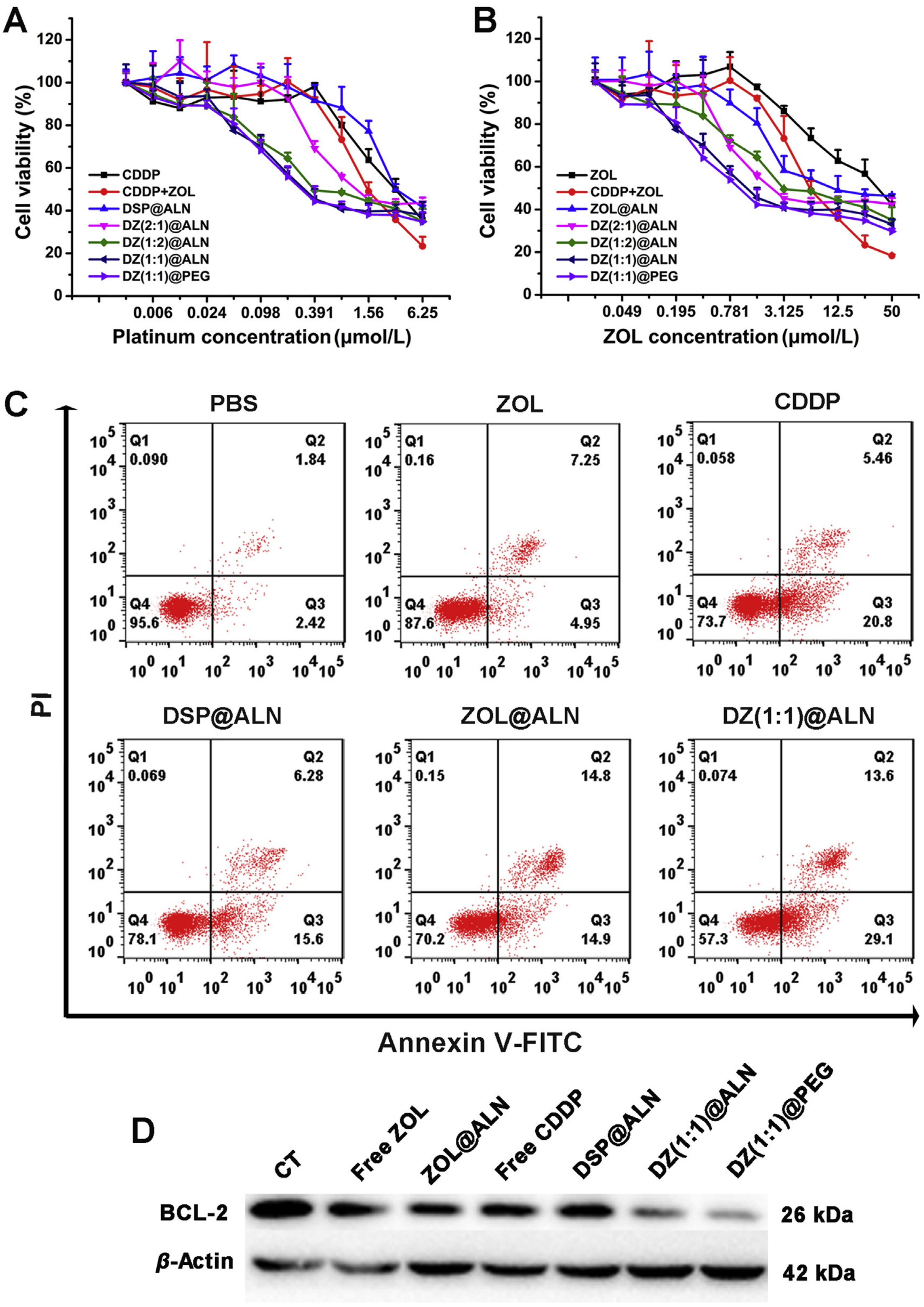

Figure 3 (A) and (B) *In vitro* cell cytotoxicity of different drug formulations against MDA-MB-231 cells after 72 h incubation. Data were expressed as mean ± SD ($n = 6$). (C) Annexin V-FITC/PI assay for apoptosis detection of MDA-MB-231 cells after treated with different drug formulations. (D) Western blot analysis of apoptosis-related protein BCL-2 in MDA-MB-231 cells.

To further verify the bone targeting ability of DZ(1:1)@ALN, the periostea stripped mouse skull bones were incubated with free DiI and DiI-labeled nanoparticles, and the samples were imaged using fluorescence microscopy. The intensity of fluorescence indicates the capacity of binding affinity. Free DiI and DZ(1:1)@PEG did not show any specific binding to bone fragments, displaying similar fluorescence intensity as the PBS group (Supporting Information Fig. S3). However, DZ(1:1)@ALN showed superior bone fragments binding ability than DZ(1:1)@PEG due to the ALN spreading on the surface, which was consistent with the HA binding experiment. These results demonstrated that ALN functionalization endowed DZ(1:1)@ALN with better bone affinity, indicating the superior *in vivo* bone-targeting ability to promote the therapeutic effect.

3.4. *In vitro therapeutic effect*

The cytotoxicity of various formulations against triple-negative breast cancer cell lines of human MDA-MB-231 and murine 4T1 cells were evaluated for 72 h using MTT assay. All drug formulations displayed enhanced cytotoxicity to both MDA-MB-231 and 4T1 cells with increasing incubation concentrations (Fig. 3A and B, Supporting Information S4A and S4B). The IC_{50} values calculated from the dose responsive curve were summarized in Table 2. Monotherapeutic DSP@ALN showed comparable cytotoxicity as free CDDP, with $IC_{50,Pt} = 4.18$ μmol/L against MDA-MB-231 cells. ZOL@ALN showed increased cytotoxicity compared with free ZOL, with IC_{50} value about 2-fold lower than free ZOL, which may be due to the strong polarity of free ZOL which hindered cellular uptake. DZ(2:1)@ALN, DZ(1:1)@ALN and DZ(1:2)@ALN exhibited significantly enhanced anticancer effect against MDA-MB-231 and 4T1 cells, their IC_{50} values of the two drugs were significantly decreased, indicating the synergistic cytotoxic effect.

To further study the synergistic effect of DZ@ALN to screen an optimal drug formulation, the CI values of DZ(2:1)@ALN, DZ(1:1)@ALN and DZ(1:2)@ALN were determined according to the formula described in the method section, and were summarized in Table 2. The CI value below 1 indicated the synergistic effect between CDDP and ZOL in nanoparticles. DZ(1:1)@ALN had the smallest CI value than DZ(2:1)@ALN and DZ(1:2) @ALN, indicating the strongest synergistic effect. Similarly, the synergistic effect in 4T1 cells exhibited the same results. Therefore, DZ(1:1)@ALN were chosen for the follow-up study, and the cytotoxicity of DZ(1:1)@PEG and free drug combinations corresponding to the drug ratio in DZ(1:1)@ALN were investigated in MDA-MB-231 and 4T1 cells. DZ(1:1)@PEG showed comparable cytotoxicity with DZ(1:1)@ALN, with similar IC_{50} and CI value, revealing that the bone-targeting or non-targeting material modification had no influence on cytotoxicity under the treated dose. Free drug combination also showed synergistic cytotoxicity compared with free CDDP and ZOL alone.

The synergistic effect between CDDP and ZOL might be caused by the control of cell proliferation. CDDP can inhibit cell proliferation by interfering with DNA replication *via* forming DNA adduct[45]. ZOL could inhibit a key enzyme, farnesyl pyrophosphate synthase (FPPS), in the mevalonate pathway, leading to isopentenyl diphosphate (IPP) accumulation and the formation of cytotoxic ATP analogue, eventually inducing cells apoptosis (*i.e.*, cancer cells and osteoclasts)[46]. ZOL has been reported to down-regulate the expression of p-MAPK, MCL-1, p-mTOR. p-MAPK is a part of mevalonate pathway, MCL-1 is involved in cell cycle and proliferation and mTOR is critically participate in cell survival and proliferation[47–49]. Because the mTOR pathway is responsive for the resistance of chemotherapeutic drugs, studies found that inhibiting the mTOR pathway could overcome MDA-MB-231 cells resistance to CDDP, since ZOL has the ability to enhance mTOR inhibition, thereby overcoming resistance to CDDP, realizing the synergistic inhibitory of cell proliferation in MDA-MB-231 cells[47,50,51]. Combining CDDP and ZOL in one single nanoagent brings the benefits of single drugs together, and the same cytotoxicity effect can be achieved with reduced doses of both drugs, thus reducing systemic cytotoxicity.

To further confirm the synergistic effect of DZ(1:1)@ALN on inducing apoptosis, FCM analysis was performed toward MDA-MB-231 cells at an equivalent dose of CDDP (3.125 μmol/L) and ZOL (12.5 μmol/L) for 48 h treatment. DZ(1:1)@ALN showed the highest ability to induce cell apoptosis, resulting in 42.7% apoptotic cells, and DZ(1:1)@PEG showed comparable apoptotic cells (Fig. 3C and Fig. S4C). Single drug DSP@ALN showed comparable apoptotic cells with free CDDP, with 21.9% and 26.3% apoptotic cells, respectively. Single drug ZOL@ALN showed more apoptotic cells than free ZOL, with 12.4% and 29.8%, respectively. Almost no apoptotic cells were observed in PBS group. These results were in consistent with the cytotoxicity assay and strongly indicated the remarkable cytotoxic effect of DZ(1:1)@ALN than free drug or monotherapeutic nanoparticles. Western blot analysis of the expression of BCL-2 (an antiapoptotic protein) further confirmed that DZ(1:1)@ALN and DZ(1:1)@PEG had the optimal capacity to trigger cell apoptosis, with the least expression of BCL-2 compared with the free drug and monotherapeutic nanoparticles (Fig. 3D).

3.5. *In vitro osteoclasts inhibition*

Previous studies reported that bone tumors could dysfunctional bone marrow microenvironment, resulting in the recruitment of osteoclast progenitors, which further activated into mature osteoclasts *via* osteoclastic activating factors secreted by tumor cells, and osteoclast-mediated bone resorption leading to osteolysis3.

Table 2 The IC_{50} and CI values of various drug formulations against MDA-MB-231, 4T1 and RAW 264.7 cells after incubation for 72 h.

Drug	MDA-MB-231 (μmol/L)			4T1 (μmol/L)			RAW 264.7 (μmol/L)		
	$IC_{50,Pt}$	$IC_{50,ZOL}$	CI	$IC_{50,Pt}$	$IC_{50,ZOL}$	CI	$IC_{50,Pt}$	$IC_{50,ZOL}$	CI
CDDP	3.30	–	–	3.75	–	–	1.28	–	–
ZOL	–	52.50	–	–	3.80	–	–	25.79	–
CDDP+ZOL	1.99	8.14	0.76	0.37	1.47	0.48	0.82	3.31	0.78
DSP@ALN	4.18	–	–	7.64	–	–	2.08	–	–
ZOL@ALN	–	24.30	–	–	2.53	–	–	2.23	–
DZ(2:1)@ALN	2.36	5.61	0.79	0.63	1.26	0.58	–	–	–
DZ(1:2)@ALN	0.97	7.78	0.55	0.21	1.69	0.69	–	–	–
DZ(1:1)@ALN	0.94	3.98	0.39	0.27	1.09	0.47	0.23	0.99	0.56
DZ(1:1)@PEG	0.77	2.79	0.30	0.26	1.03	0.44	0.25	0.92	0.52

– Not applicable. Data were presented as mean ± SD ($n = 6$).

The "vicious cycle" between tumor cells and osteoclasts lead to both osteolysis and tumor growth, thus, in addition to inhibiting tumor cells, inhibition of osteoclasts is equally important. As osteoclasts were derived from osteoclast progenitors under the stimulation of various cytokines in the bone metastatic environment, the inhibition of osteoclast progenitors RAW 264.7 cells by DZ(1:1)@ALN was preliminarily investigated using MTT method. Similar to cytotoxicity against tumor cells, all drug formulations displayed enhanced effect with increasing dose (Fig. 4A). The IC_{50} values were summarized in Table 2. DZ(1:1)@ALN showed significantly enhanced effect, with $IC_{50,pt}$ ($IC_{50,zol}$) = 0.23 (0.99) μmol/L, 9- and 2.2-fold lower than that of monotherapeutic DSP@ALN and ZOL@ALN, respectively. In addition, free CDDP and ZOL combination displayed synergistic cytotoxic effect, and the CI values of free drug counterparts and DZ(1:1)@ALN were 0.78 and 0.56, respectively.

To further confirm the synergistic effect of DZ(1:1)@ALN on inducing apoptosis of RAW 264.7 cells, FCM analysis was performed at an equivalent dose of CDDP (1.56 μmol/L) and ZOL (6.25 μmol/L) of free drugs or nanoparticles for 48 h treatment. DZ(1:1)@ALN showed the highest ability to induce cell apoptosis, resulting in 68.10% apoptotic cells, higher than the single drug DSP@ALN and ZOL@ALN, with 34.5% and 57.3% apoptotic cells, respectively (Fig. 5A). These results indicated the remarkable cytotoxic effect of DZ(1:1)@ALN than monotherapeutic nanoparticles toward osteoclast progenitors.

To assess the biological activity of DZ(1:1)@ALN on inhibiting osteoclasts differentiation, osteoclast progenitors RAW 264.7 cells were co-incubation with varying drug formulations containing 50 ng/mL RANKL. An equivalent dose of CDDP (0.781 μmol/L) and ZOL (3.12 μmol/L) was adopted to study their inhibition effect on osteoclasts differentiation. Fig. 4C and the quantification of the multinucleated ($n \geq 3$) osteoclastic-like cell per representative view stained by TRAP (Fig. 4B) exhibited that DZ(1:1)@ALN had the most effective inhibitory effect on the differentiation of osteoclasts compared with all other groups, and DZ(1:1)@PEG showed comparable effect, indicating that the bone-seeking material had no effect on osteoclasts differentiation under the current dose.

Osteoclasts after treated with various drug formulations.

The effect of DZ(1:1)@ALN on inducing osteoclasts apoptosis was further investigated by FCM. An equivalent dose of CDDP (1.56 μmol/L) and ZOL (6.25 μmol/L) was adopted to study osteoclasts apoptosis under 48 h incubation. DZ(1:1)@ALN showed the strongest effect on inducing apoptosis of osteoclasts, resulting in 64.20% apoptotic cells, higher than the single drug DSP@ALN

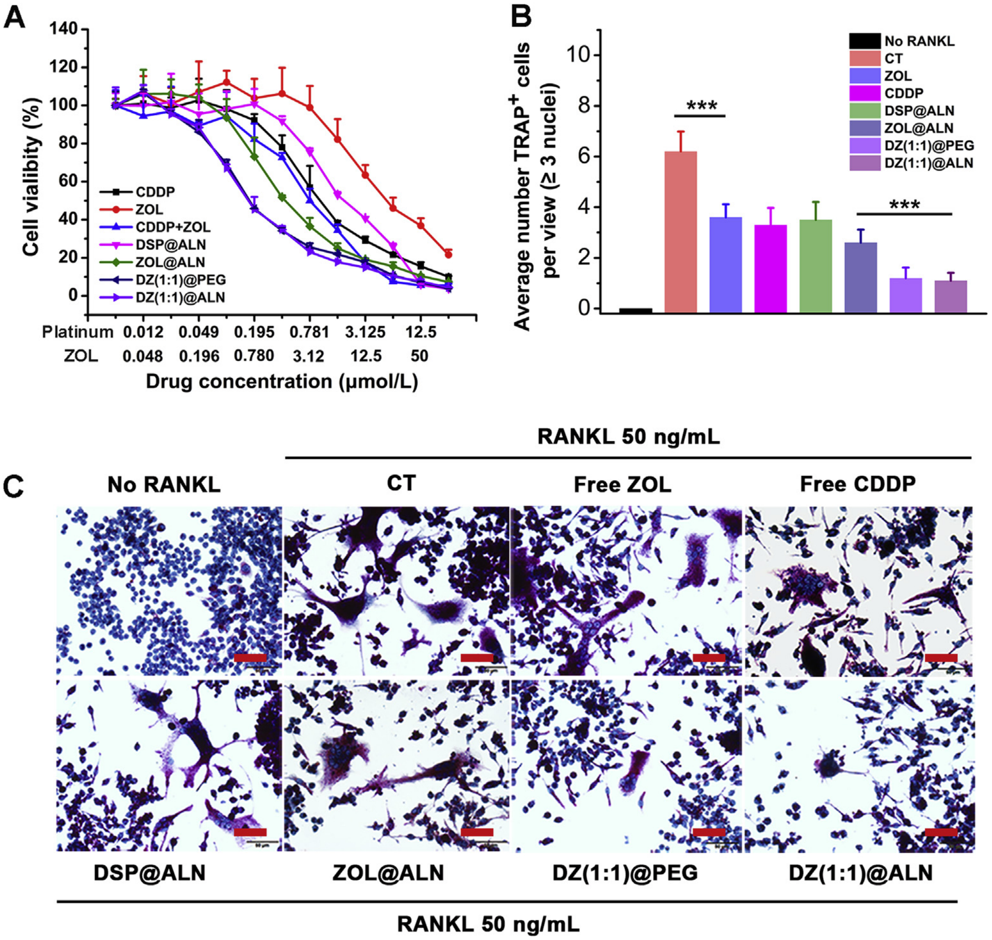

Figure 4 (A) *In vitro* cell cytotoxicity of different drug formulations against RAW 264.7 cells after 72 h incubation. Values were expressed as mean ± SD ($n = 6$). (B) Quantitative analysis of average TRAP positive cells per representative view. $^{***}P < 0.001$. (C) Representative microscopy images of osteoclasts differentiation stimulated by RANKL (50 ng/mL) containing different drug formulations. Osteoclasts were stained in purple. Scale bar: 50 μm.

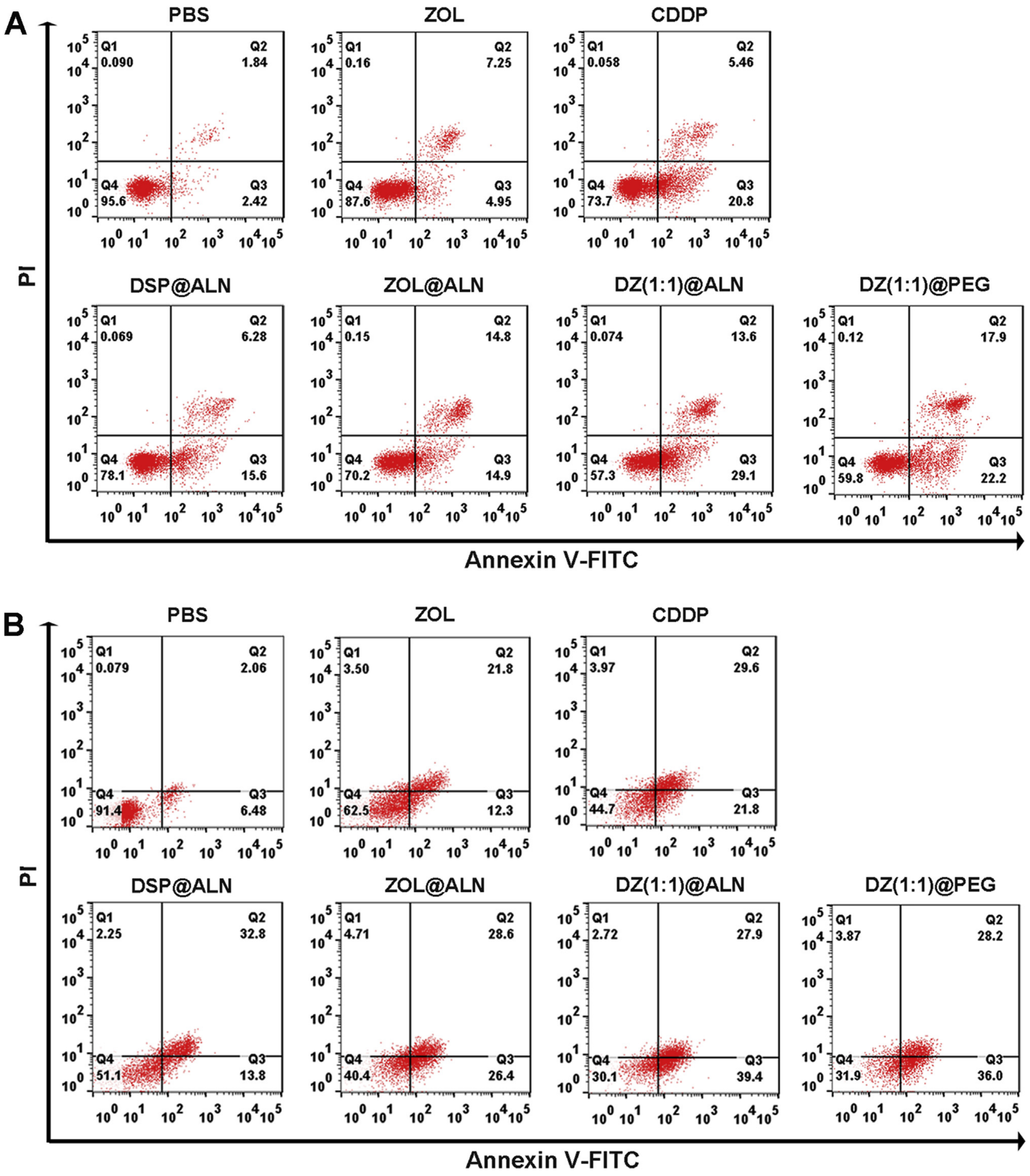

Figure 5 Annexin V-FITC/PI assay for apoptosis detection of (A) RAW 264.7 cells and (B) Osteoclasts after treated with various drug formulations.

and ZOL@ALN, with 46.60% and 55.00% apoptotic cells, respectively (Fig. 5B), indicating the remarkable cytotoxic effect of DZ(1:1)@ALN toward osteoclasts.

All of this results revealed that DZ(1:1)@ALN could not only synergistically inhibit tumor cells, but also inhibit the three steps which osteoclasts play their roles, including inhibiting osteoclast progenitors, osteoclasts differentiation and inducing osteoclasts apoptosis, which was expected to breakdown the "vicious cycle" for effective bone metastasis treatment.

3.6. *In vivo pharmacokinetics and biodistribution study*

The blood clearance of free CDDP, DZ(1:1)@PEG and DZ(1:1)@ALN were investigated on SD rats by single intravenous

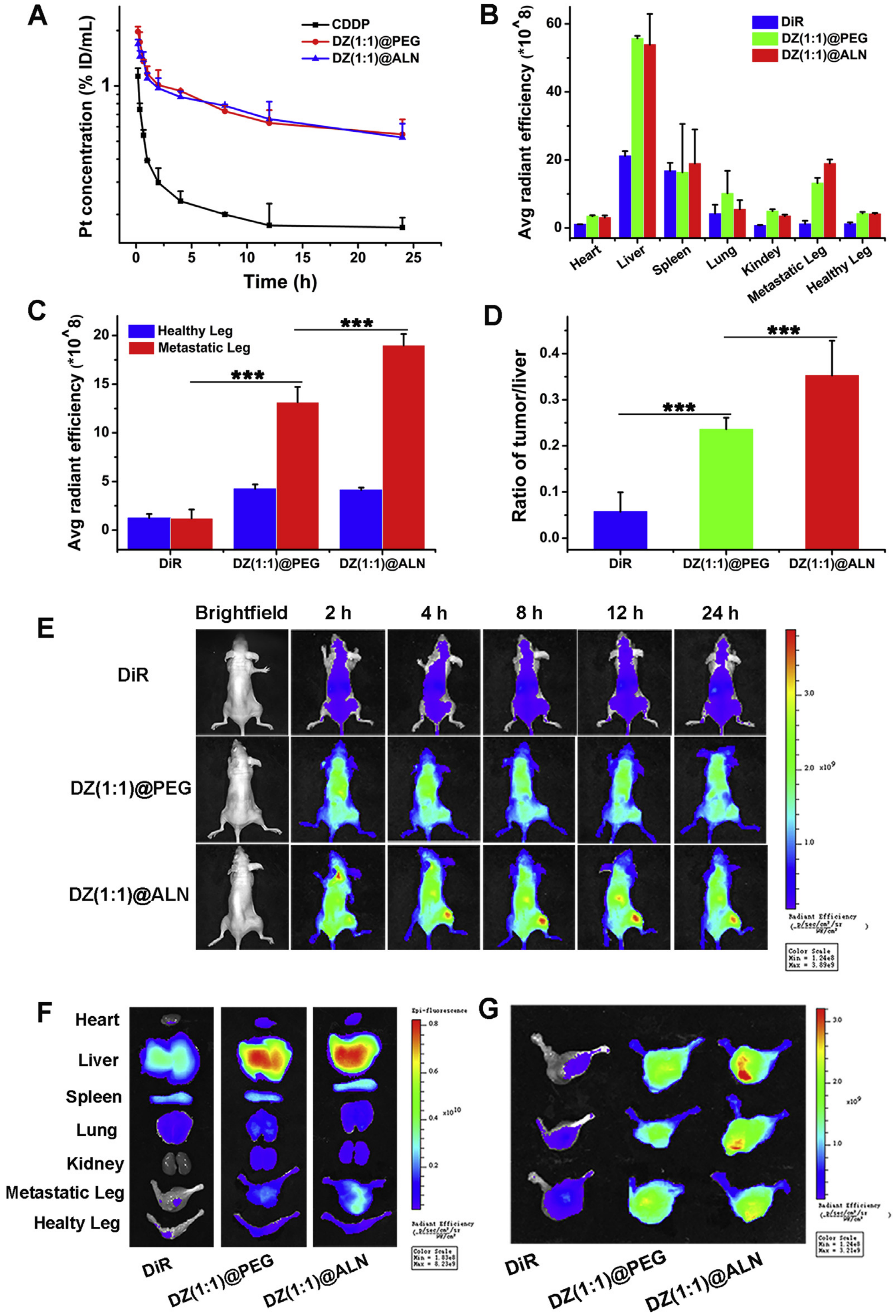

Figure 6 (A) Pharmacokinetics of CDDP, DZ(1:1)@PEG and DZ(1:1)@ALN in SD rats from 0 to 24 h after intravenous injection. Values were represented as mean ± SD ($n = 3$). (B) Fluorescence quantitative assessment of major organs, healthy legs, and metastatic legs collected at 24 h post-injection. (C) Fluorescence quantitative assessment of metastatic legs collected at 24 h post-injection. (D) Metastatic leg:liver ratios quantified by DiR fluorescence at 24 h post-injection. (E) *In vivo* imaging of free DiR, DiR labeled DZ(1:1)@PEG and DZ(1:1)@ALN after vein injection to bone metastatic BALB/c-*nu*/*nu* mice. (F) *Ex vivo* fluorescence images of major organs, healthy leg, and bone metastatic leg of the representative mice after 24 h injection. (G) Fluorescence images of metastatic legs. Values were presented as mean ± SD ($n = 3$, $^{***}P < 0.001$).

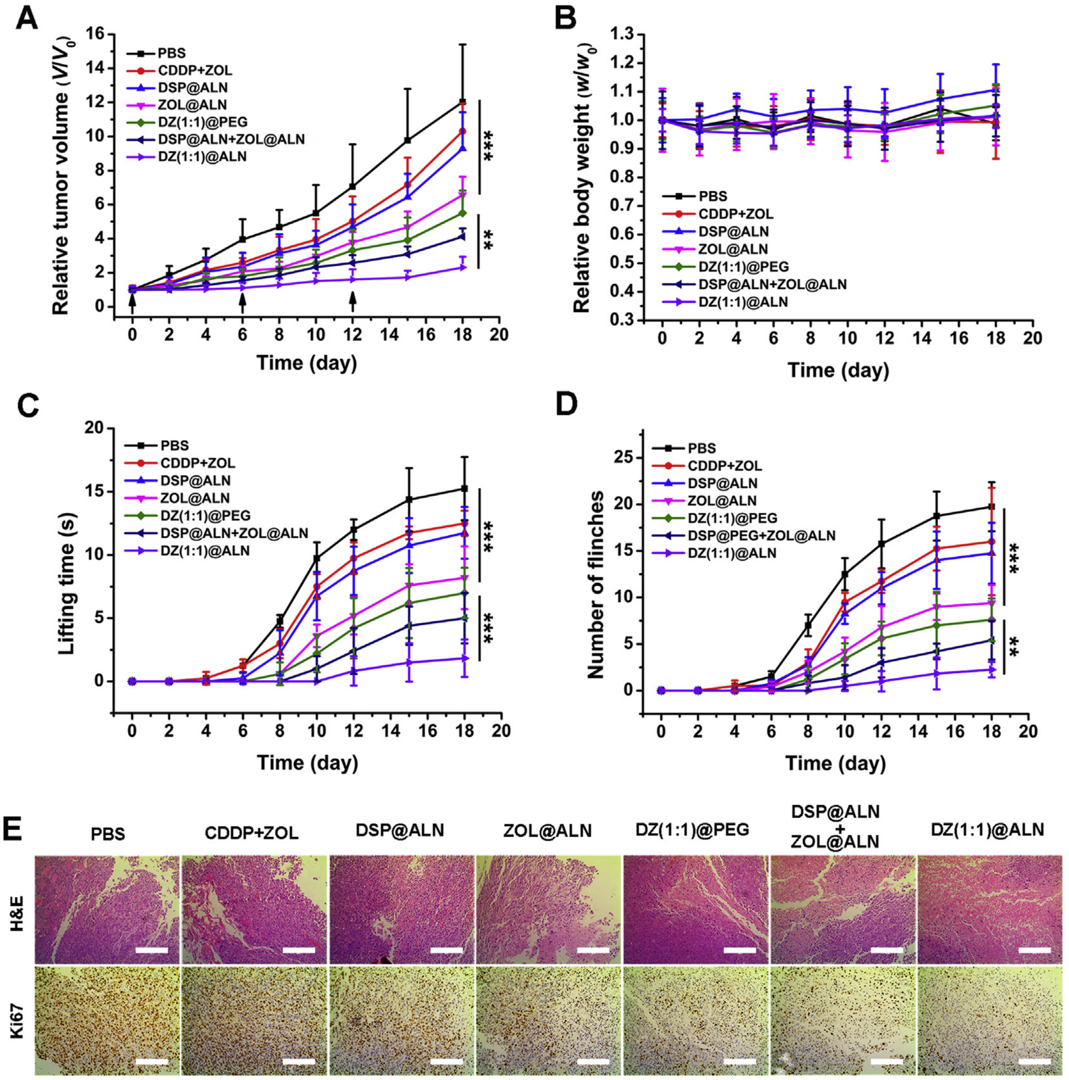

Figure 7 Evaluation of tumor growth and bone pain inhibition. (A) Relative tumor volumes and (B) Relative body weight of different treatment groups. (C) Spontaneous lifting time and (D) Number of flinches of the bone metastatic hindlimb. The arrows indicated the day of tail vein injection. Values were expressed as mean ± SD ($n = 6$, $^{**}P < 0.01$, $^{***}P < 0.001$). (E) H&E and Ki67 staining of the tumor tissues after various treatments. Scale bar: 200 μm.

injection, the platinum concentration in plasma were measured by GFAAS. Free CDDP displayed rapid plasma clearance behavior after intravenous injection (Fig. 6A). In contrast, DZ(1:1)@ALN and DZ(1:1)@PEG showed a significant longer blood circulation time than CDDP, suggesting that the nanoparticles may have the ability to escape the reticuloendothelial system (RES) uptake and facilitate the tumor accumulation by enhanced penetration and retention effect.

To investigate the specific accumulation of DZ(1:1)@ALN in bone metastatic lesions, fluorescence imaging was performed and the drug concentrations in tissues were detected. For fluorescence imaging studies, free DiR showed non-specific distribution during the observation, with the fluorescence intensity highest in liver, and only a small amount was detected in the bone tumor (Fig. 6E). By contrast, evident fluorescence signals were observed in tumors as early as 2 h in both DZ(1:1)@PEG and DZ(1:1)@ALN, which maintained or increased over time, this may be due to the enhanced penetration ability of nanoparticles due to their small particle sizes. And it was notably that the fluorescence intensity in DZ(1:1)@ALN was significantly higher than DZ(1:1)@PEG at all determined times, especially after 2 h injection, indicating that ALN functionalization endowed the bone-seeking capacity of DZ(1:1)@ALN.

Ex vivo fluorescence imaging of major organs and right hindlimbs (bone metastatic legs) at 24 h post injection also confirmed the strongest targeting capability of DZ(1:1)@ALN than DZ(1:1)@PEG and free DiR (Fig. 6B, F and 6G). Meanwhile, when compared the quantitate fluorescence intensity of bone metastatic hindlimb with their opposite left hindlimb (Fig. 6C), free DiR showed no significant difference, while DZ(1:1)@ALN showed 4.6-fold higher, revealing that DZ(1:1)@ALN could selectively localized to the bone metastatic site. Besides, the fluorescence images of *ex vivo* tissues also exhibited dominant liver accumulation, as reported by other studies[52,53]. Therefore, the quantification fluorescence intensity of bone:liver was performed, DZ(1:1)@ALN showed significantly higher bone:liver than DZ(1:1)@PEG (Fig. 6D).

The drug content in organs and tissues was further detected by GFAAS. Free CDDP was distributed rapidly to each tissue within

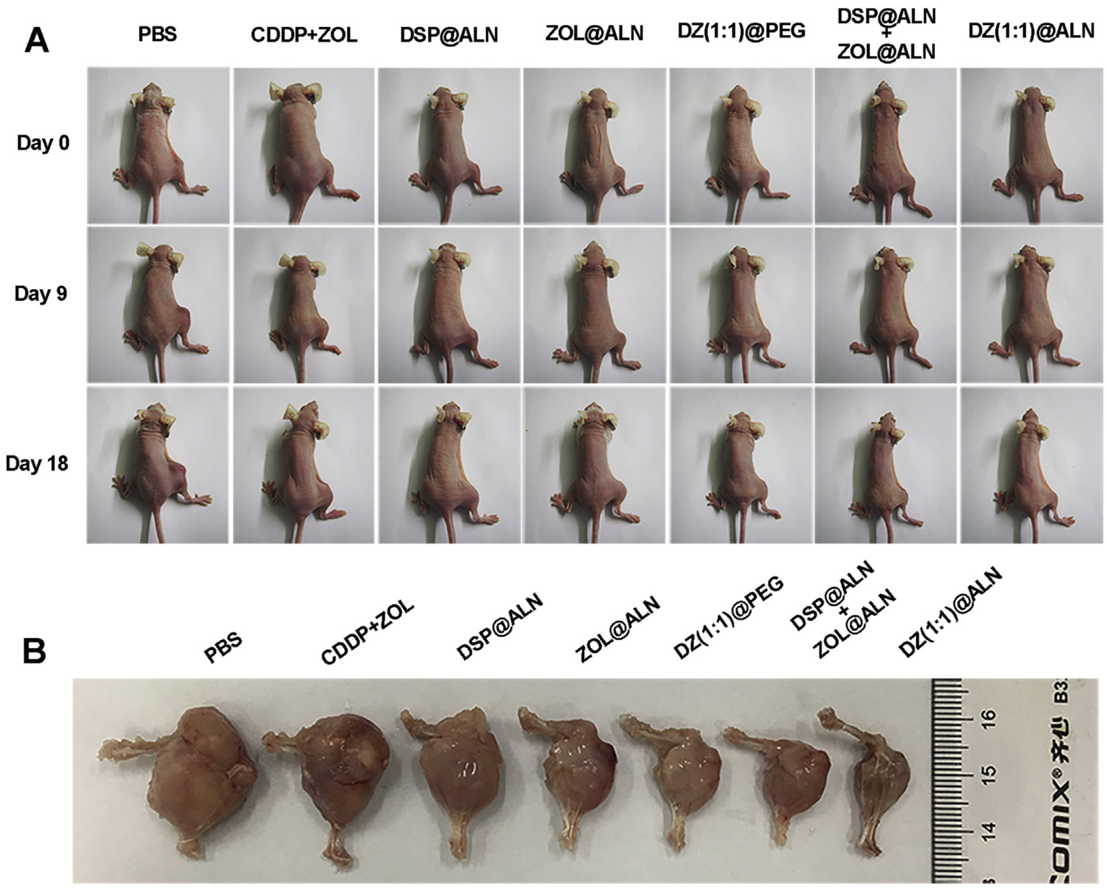

Figure 8 (A) Photograph of bone metastatic mice on Days 0, 9 and 18. (B) *Ex vivo* photos of the representative bone metastatic hindlimbs of different groups.

15 min, the platinum concentration in kidneys was the highest at 15 min post-injection, and it was eliminated from the body with time increasing (Supporting Information Fig. S5A). The platinum content of DZ(1:1)@PEG (Fig. S5B) in bone metastatic leg were higher than CDDP and the contralateral healthy leg. This might be due to the enhanced penetration and retention effect. However, significantly increased platinum content of DZ(1:1)@ALN in bone metastatic leg was observed (Fig. S5C), which was about 2.06-fold higher than that in the healthy leg, and 2.11-fold than that of DZ(1:1)@PEG at 15 min post-injection, and the platinum content was gradually accumulated with time went on. This was ascribed to the natural bone-seeking ability of ALN and its preferential distribution to bone metastatic lesions[54].

All of these results confirmed that DZ(1:1)@ALN could preferentially accumulate in bone metastatic lesion, which would lead to the improved *in vivo* efficacy and reduced systemic toxicity.

3.7. *In vivo therapeutic effect*

3.7.1. *Tumor growth inhibition*

Intra-tibia injection of MDA-MB-231 cells was used to establish the model of bone metastasis from breast cancer, which is valid for investigating the interactions of cancer cells with the bone microenvironment[55]. Compared with PBS group, all the other treatment groups were showed a decrease in tumor growth (Figs. 7A and 8A). Mice treated with DZ(1:1)@ALN showed the most prominent cancer inhibition compared to the other treatment groups, with average tumor size about 5.5-fold smaller than PBS group at the end of experiment, likely due to the favorable pharmacokinetics profiles, selective distribution to the metastatic bone and the simultaneous release of the two drugs to realize the optimal synergistic therapeutic effect. Free CDDP+ZOL group displayed a poor therapeutic effect, possibly due to rapid clearance in plasma after injection. Though free ZOL could selectively distribute to bone, CDDP had no bone-seeking ability, resulting in the out of sync distribution behavior of the two drugs, thereby reducing the synergistic effect. ZOL@ALN group showed moderate tumor inhibition effect, possibly due to that when ZOL constructed into nanoparticles, it possessed comparatively excellent pharmacokinetics profiles than free ZOL, under the guidance of ALN, ZOL@ALN could selectively accumulated to bone metastatic lesion, underwent pH triggered ZOL release, the released ZOL could one part interfer the function of osteoclasts, broke the "vicious circle" to some extent and the other part inhibit the tumor cells. DZ(1:1)@PEG group showed a little better tumor suppression effect than that of ZOL@ALN, possibly caused by the synergistic effect of CDDP and ZOL co-delivered by the same nanoagent, though DZ(1:1)@PEG only possessed passive targeting ability, it's effect still better than the active targeted monotherapy nanoagent. DSP@ALN+ZOL@ALN group that co-delivered CDDP and ZOL separately from two nanoagent showed weaker tumor inhibition effect than DZ(1:1)@ALN group that co-delivered CDDP and ZOL in the same system. This may be

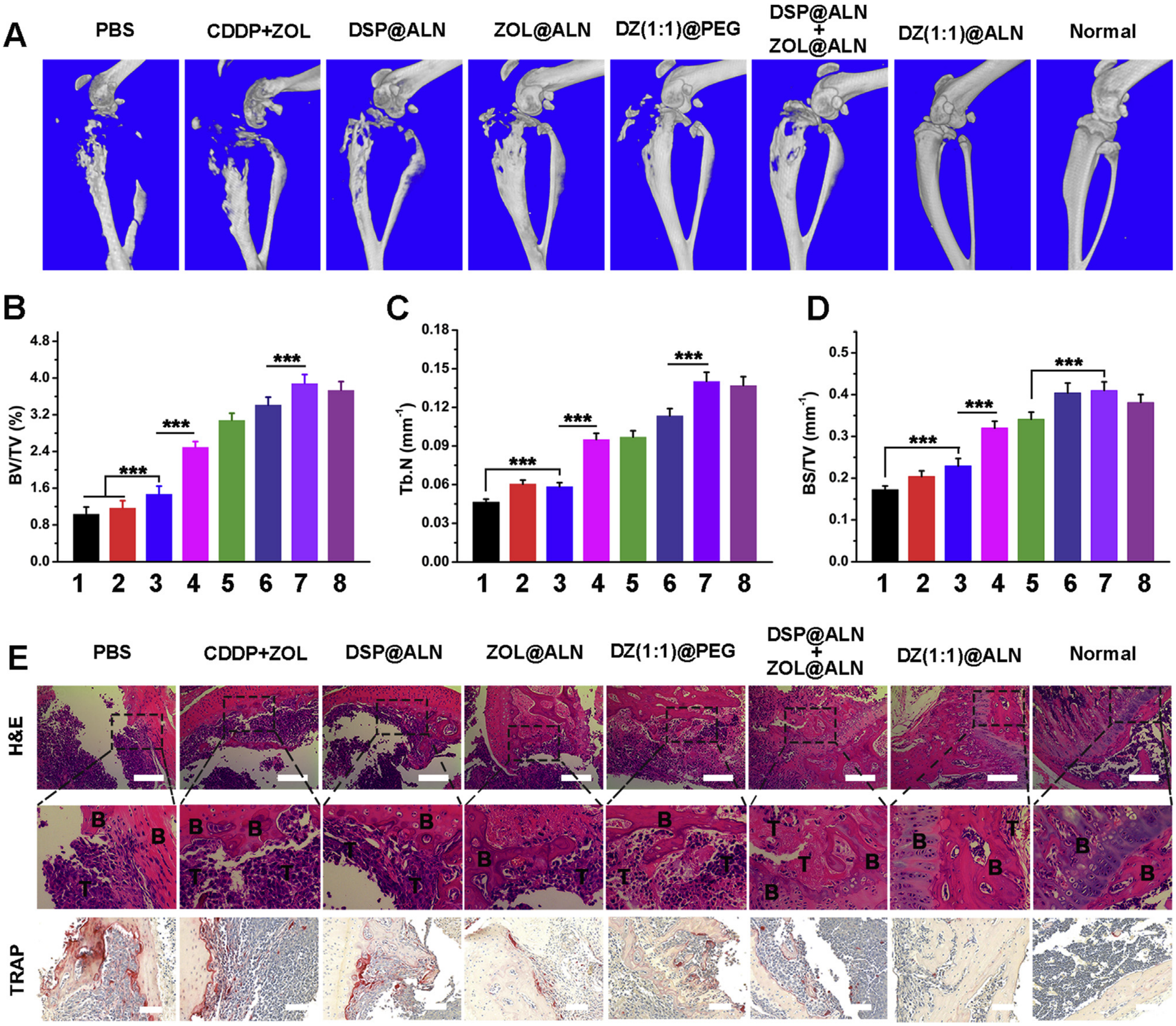

Figure 9 Evaluation of osteolysis inhibition. (A) 3D micro-CT reconstruction image of the mice tibias. The architecture parameters of (B) BV/TV, (C) Tb.N and (D) BS/TV after various treatments (1: PBS; 2: CDDP+ZOL; 3: DSP@ALN; 4: ZOL@ALN; 5: DZ(1:1)@PEG; 6: DSP@ALN+ZOL@ALN; 7: DZ(1:1)@ALN and 8: Normal). (E) H&E and TRAP staining of the tumor-bearing tibias. B represents bone and T represents tumor. Scale bar was 200 and 100 μm for H&E and TRAP, respectively. Values were presented as mean ± SD ($n = 6$, $^{**}P < 0.01$, $^{***}P < 0.001$).

due to that co-deliver of two drugs in one nanoagent could normalize pharmacokinetics, selective distribution behavior and the controlled drug release in target site, thus realizing the optimal synergistic therapeutic effect.

The representative *ex vivo* tumors of each groups were photographed, and the results were consistent with the caliper measures (Fig. 8B). In addition, no obvious body weight loss in all treatment groups were observed (Fig. 7B), suggesting negligible systemic toxicity during the current dosage and dosing schedules. The antitumor efficacy was further verified by H&E and Ki67 staining of tumor tissues (Fig. 7E), the H&E staining result showed that a large amount of cell necrosis with nuclear shrinkage and nucleoplasm atrophy occurred in DZ(1:1)@ALN group than the other groups, further indicating the strongest tumor suppression effect. Ki67 is a cellular proliferation marker, and the decrease of Ki67 indicates the proliferation of tumor cell is inhibited[56]. DZ(1:1)@ALN group exhibited the lowest Ki67 staining cells, which was consistent with the H&E staining.

3.7.2. *Bone pain remission*

Bone pain is a frequent symptom of patients with metastatic bone disease[57]. It was evaluated by recording spontaneous lifting time and the number of flinches of the tumor bearing hindlimb over a 5-min period. The spontaneous lifting time of all treatment group gradually increased over time, obvious difference between different treatment groups was first observed on Day 10, and maximum difference was observed on Day 18 (Fig. 7C and D). Though all the treatment groups could relieve bone pain compared with PBS group, comparatively, DZ(1:1)@ALN group showed spontaneous lifting behavior on Day 12 and the lifting time was the shortest (1.75±0.86 s on Day 18) among other groups. The number of flinches showed the similar results. Both of the results

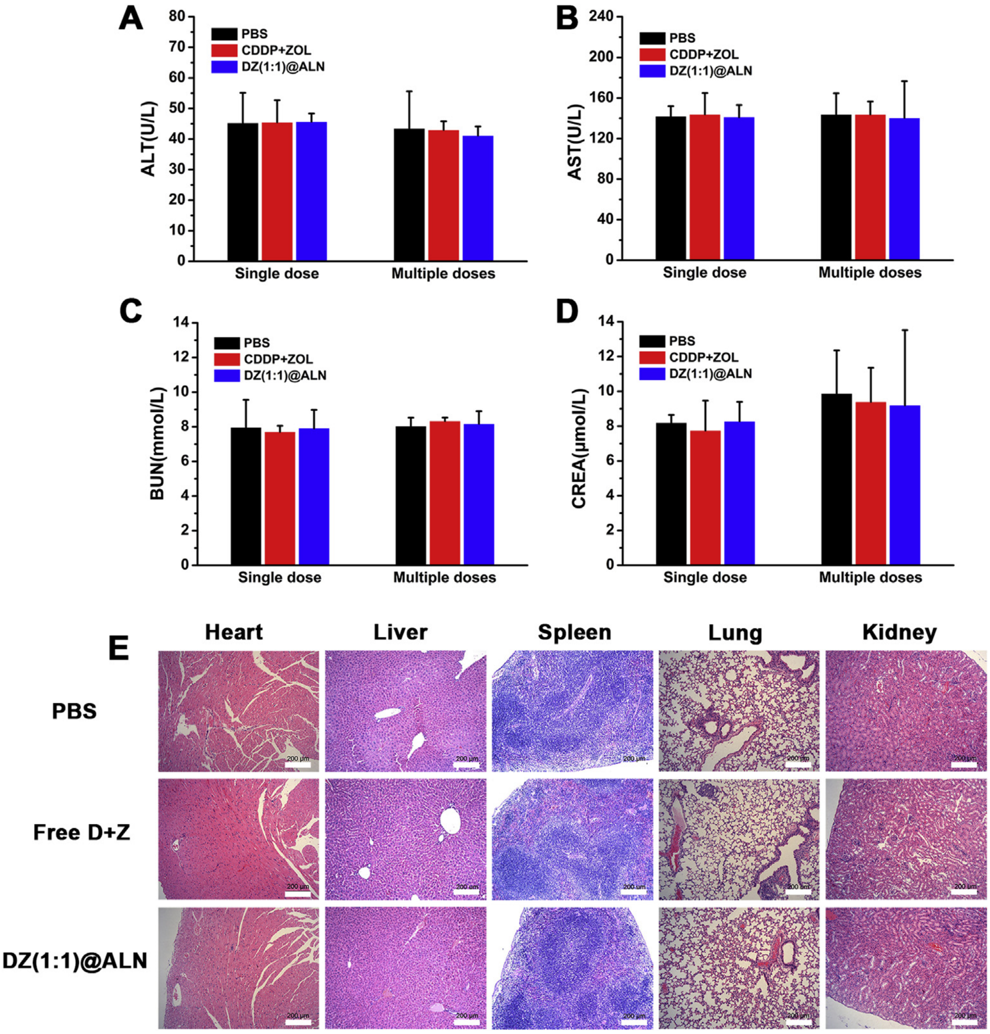

Figure 10 (A)−(D) Blood biochemistry indexes including liver-function markers: ALT, AST, and kidney-function markers: BUN, CREA. Data were expressed as mean ± SD ($n = 6$). (E) H&E staining images of main organs after multiple doses injection. Scale bar: 200 μm.

suggested that DZ(1:1)@ALN could effectively alleviate bone pain, eventually improving the patients' quality of life.

3.7.3. *Osteolysis inhibition*

After the evaluation of the tumor inhibition effect, the inhibition effect of DZ(1:1)@ALN on bone metastasis induced osteolysis was further investigated by 3D micro-CT. The proximal tibias in PBS, free CDDP+ZOL and DSP@ALN groups showed comminuted fractures (Fig. 9A). While the tibias in mice treated with monotherapy or dual therapy nanoparticles containing ZOL were less destructed, and it is exciting that the osteolysis was significantly relieved in DZ(1:1)@ALN group, with the morphology and structure of the tibias similar to the normal tibia (without implanted tumor cells). In addition, the bone parameters of the tibias such as BV/TV, Tb. N and BS/TV were summarized in Fig. 9B−D. BV/TV or Tb. N reflects the bone resorption extent, with the lower the BV/TV or Tb. N value, the greater the bone resorption extent. DZ(1:1)@ALN group showed the highest BV/TV and Tb. N value which were comparable to the normal tibias. The results of BS/TV values showed the similar trend. These results implied that DZ(1:1)@ALN could significantly inhibit osteolysis *in vivo*.

The damage extent of metastatic tibias was further investigated by H&E staining. The tibial cortical bone, cartilage and sclerotin of knee joint, bone trabecular and bone marrow cavity in PBS, free CDDP+ZOL and DSP@ALN groups were severely damaged, and replaced by proliferating tumor cells (Fig. 9E). Compared with the above three groups, ZOL@ALN, DZ(1:1)@PEG and ZOL@ALN+DSP@ALN group showed relatively less extensive osteolysis. However, the osteolysis in the DZ(1:1)@ALN group seemed to be suppressed, and bone structure was better maintained compared with other groups. At the meanwhile, the contralateral tibia of the same mice in DZ(1:1)@ALN group was also compared (Supporting Information Fig. S6A), which appeared almost the same as the normal tibia. The H&E staining results uncovered that DZ(1:1)@ALN possessed the potent potential for preventing osteolysis without inducing side effect in uninfected bone tissues.

As TRAP is the biomarkers for osteoclasts that reflect the bone resorption *in vivo*[58,59], to further confirm the relief of bone destruction by DZ(1:1)@ALN was owing to the synergistic inhibitory effect of osteoclasts activation, TRAP staining was performed in bone metastatic tibias. Consistent with the severity degree of osteolysis, PBS, CDDP+ZOL and DSP@ALN group showed a large amount of osteoclasts, the monotherapy ZOL@ALN and DZ(1:1)@PEG showed moderate osteoclasts, while DZ(1:1)@ALN showed significantly reduced TRAP positive osteoclasts, possibly due to the dual function of active targeting and drug combination therapy (Fig. 9E). The TRAP staining of the contralateral tibia (without tumor) of the same mice in DZ(1:1)@ALN group was also compared (Fig. S6B), which appeared almost the same as the normal tibia, suggesting neglectable effect to healthy bone tissues.

All of these results *in vivo* reveled that DZ(1:1)@ALN could not only synergistically inhibit the proliferation of tumor cells, relieve the bone pain of bone metastatic mice, but also synergistically inhibit the activation of osteoclasts, protect the bone from damage. As cancer cells and osteoclasts supplement each other in bone microenvironment, leading to a “vicious cycle” that exacerbate bone metastasis, the potent effect of DZ(1:1)@ALN to inhibit tumor cells and osteoclasts could breakdown the “vicious cycle” to some extent, eventually reducing tumor burden and osteolysis. However, the detailed intracellular synergistic inhibition mechanism of CDDP and ZOL will be further elaborated in the future studies.

3.8. *Safety evaluation*

To evaluate the systemic toxicity, the liver biochemical parameters ALT and AST, kidney biochemical parameters BUN and CREA were determined. Mice treated with PBS were used as control. The above biochemical parameters of free CDDP + ZOL and DZ(1:1)@ALN groups exhibited no significant difference compared with PBS group no matter single or multiple dose injection, suggesting no significant damage to the liver and kidney under the current dosage (Fig. 10A−D). No apparent histomorphological changes (Fig. 10E) were observed in major organs of DZ(1:1)@ALN group compared with PBS group. The preliminary data revealed that DZ(1:1)@ALN had no noticeable toxicity at the given dose *in vivo* while maintaining favorable therapeutic effect due to the synergistic effect of CDDP and ZOL.

4. Conclusions

In summary, a bone-seeking nanoplatform which co-delivers CDDP and ZOL for synergistic treatment of bone metastatic breast cancer has been successfully constructed. DZ(1:1)@ALN with reaction molar ratio DSP/ZOL = 1:1 was selected for its strongest cytotoxicity against MDA-MB-231 cells. DZ(1:1)@ALN has excellent colloidal stability under physiological conditions and potent *in vitro* bone affinity. Furthermore, DZ(1:1)@ALN could synergistically inhibit MDA-MB-231 and 4T1 cells, synergistically suppress the activation and induce the apoptosis of osteoclasts *in vitro*. DZ(1:1)@ALN could significantly prolong the blood circulation time *in vivo*, and selectively accumulate in bone affected site, then release platinum drug and ZOL rapidly in a synchronous manner under the low pH microenvironment of bone metastasis, achieving the most potent effect on inhibiting tumor growth and bone resorption simultaneously. Finally, DZ(1:1)@ALN showed no noticeable toxicity at the given dose and dosing schedules. All of these results highlighted the great potential of DZ(1:1)@ALN as bone-targeted nanoplatform for effective treatment of bone metastatic breast cancer.

Acknowledgment

This work was supported by the National Natural Science Foundation of China (Grant No. 81973256/H3008).

Author contributions

Yanjuan Huang conceived the study and designed the experiments with the help from Chunshun Zhao. Yanjuan Huang, Zhanghong Xiao, Zilin Guan and Zishan Zeng conducted the experiments. All authors performed the data analysis and interpreted the results. Yanjuan Huang wrote the manuscript. All authors have read the manuscript and agreed to the conclusion.

Conflicts of interest

The authors declare no competing financial interest.

Appendix A. Supporting information

Supporting data to this article can be found online at https://doi.org/10.1016/j.apsb.2020.06.006.

References

1. Brook N, Brook E, Dharmarajan A, Dass CR, Chan A. Breast cancer bone metastases: pathogenesis and therapeutic targets. *Int J Biochem Cell Biol* 2018;**96**:63−78.
2. Weilbaecher KN, Guise TA, McCauley LK. Cancer to bone: a fatal attraction. *Nat Rev Canc* 2011;**11**:411−25.
3. Mundy GR. Metastasis: metastasis to bone: causes, consequences and therapeutic opportunities. *Nat Rev Canc* 2002;**2**:584−93.
4. Suvannasankha A, Chirgwin JM. Role of bone-anabolic agents in the treatment of breast cancer bone metastases. *Breast Cancer Res* 2014;**16**:484.
5. Cleeland C, von Moos R, Walker MS, Wang Y, Gao J, Chavez-MacGregor M, et al. Burden of symptoms associated with development of metastatic bone disease in patients with breast cancer. *Support Care Canc* 2016;**24**:3557−65.
6. Ren G, Esposito M, Kang Y. Bone metastasis and the metastatic niche. *J Mol Med* 2015;**93**:1203−12.
7. Coleman RE. Bone cancer in 2011: prevention and treatment of bone metastases. *Nat Rev Clin Oncol* 2011;**9**:76.
8. Subramanian G, McAfee J, Thomas F, Feld T, Zapf-Longo C, Palladino E. New diphosphonate compounds for skeletal imaging: comparison with methylene diphosphonate. *Radiology* 1983;**149**:823−8.
9. Kohno N, Aogi K, Minami H, Nakamura S, Asaga T, Iino Y, et al. Zoledronic acid significantly reduces skeletal complications compared with placebo in Japanese women with bone metastases from breast cancer: a randomized, placebo-controlled trial. *J Clin Oncol* 2005;**23**:3314−21.
10. Boissier S, Ferreras M, Peyruchaud O, Magnetto S, Ebetino FH, Colombel M, et al. Bisphosphonates inhibit breast and prostate carcinoma cell invasion, an early event in the formation of bone metastases. *Cancer Res* 2000;**60**:2949−54.
11. Saad F, Brown J, Van Poznak C, Ibrahim T, Stemmer S, Stopeck A, et al. Incidence, risk factors, and outcomes of osteonecrosis of the jaw: integrated analysis from three blinded active-controlled phase III trials in cancer patients with bone metastases. *Ann Oncol* 2011;**23**:1341−7.
12. Wang D, Lippard SJ. Cellular processing of platinum anticancer drugs. *Nat Rev Drug Discov* 2005;**4**:307−20.
13. Rosenberg B, Vancamp L, Trosko JE, Mansour VH. Platinum compounds: a new class of potent antitumour agents. *Nature* 1969;**222**:385−6.

14. Peng J, Qi T, Liao J, Chu B, Yang Q, Li W, et al. Controlled release of cisplatin from pH-thermal dual responsive nanogels. *Biomaterials* 2013;**34**:8726–40.
15. Johnstone TC, Suntharalingam K, Lippard SJ. The next generation of platinum drugs: targeted Pt (II) agents, nanoparticle delivery, and Pt (IV) prodrugs. *Chem Rev* 2016;**116**:3436–86.
16. He C, Liu D, Lin W. Nanomedicine applications of hybrid nanomaterials built from metal–ligand coordination bonds: nanoscale metal–organic frameworks and nanoscale coordination polymers. *Chem Rev* 2015;**115**:11079–108.
17. Dhar S, Daniel WL, Giljohann DA, Mirkin CA, Lippard SJ. Polyvalent oligonucleotide gold nanoparticle conjugates as delivery vehicles for platinum (IV) warheads. *J Am Chem Soc* 2009;**131**:14652–3.
18. Bi H, Dai Y, Yang P, Xu J, Yang D, Gai S, et al. Glutathione and H_2O_2 consumption promoted photodynamic and chemotherapy based on biodegradable MnO_2–Pt@ Au25 nanosheets. *Chem Eng J* 2019;**356**: 543–53.
19. Yang J, Liu W, Sui M, Tang J, Shen Y. Platinum (IV)-coordinate polymers as intracellular reduction-responsive backbone-type conjugates for cancer drug delivery. *Biomaterials* 2011;**32**:9136–43.
20. Li SL, Wang Y, Zhang J, Wei W, Lu H. Targeted delivery of a guanidine-pendant Pt (IV)-backboned poly-prodrug by an anisamide-functionalized polypeptide. *J Mater Chem B* 2017;**5**:9546–57.
21. Yu C, Ding B, Zhang X, Deng X, Deng K, Cheng Z, et al. Targeted iron nanoparticles with platinum-(IV) prodrugs and anti-EZH2 siRNA show great synergy in combating drug resistance *in vitro* and *in vivo*. *Biomaterials* 2018;**155**:112–3.
22. Rieter WJ, Pott KM, Taylor KM, Lin W. Nanoscale coordination polymers for platinum-based anticancer drug delivery. *J Am Chem Soc* 2008;**130**:11584–5.
23. Liu J, Chen Q, Zhu W, Yi X, Yang Y, Dong Z, et al. Nanoscale-coordination-polymer-shelled manganese dioxide composite nanoparticles: a multistage redox/pH/H_2O_2-responsive cancer theranostic nanoplatform. *Adv Funct Mater* 2017;**27**:1605926.
24. He Y, Huang Y, Huang Z, Jiang Y, Sun X, Shen Y, et al. Bisphosphonate-functionalized coordination polymer nanoparticles for the treatment of bone metastatic breast cancer. *J Control Release* 2017; **264**:76–88.
25. Sarin H. Physiologic upper limits of pore size of different blood capillary types and another perspective on the dual pore theory of microvascular permeability. *J Angiogene Res* 2010;**2**:14.
26. Tabrizi M, Bornstein GG, Suria H. Biodistribution mechanisms of therapeutic monoclonal antibodies in health and disease. *AAPS J* 2010;**12**:33–43.
27. Weinstein JN, Van Osdol W. Early intervention in cancer using monoclonal antibodies and other biological ligands: micropharmacology and the "binding site barrier". *Cancer Res* 1992;**52**: 2747s–51s.
28. Huang Y, He Y, Huang Z, Jiang Y, Chu W, Sun X, et al. Coordination self-assembly of platinum–bisphosphonate polymer–metal complex nanoparticles for cisplatin delivery and effective cancer therapy. *Nanoscale* 2017;**9**:10002–19.
29. Huang Z, Huang L, Huang Y, He Y, Sun X, Fu X, et al. Phthalocyanine-based coordination polymer nanoparticles for enhanced photodynamic therapy. *Nanoscale* 2017;**9**:15883–94.
30. Huang Y, Jiang Y, Xiao Z, Shen Y, Huang L, Xu X, et al. Three birds with one stone: a ferric pyrophosphate based nanoagent for synergetic NIR-triggered photo/chemodynamic therapy with glutathione depletion. *Chem Eng J* 2020;**380**:122369.
31. Huang Y, Xiao Z, Guan Z, Shen Y, Jiang Y, Xu X, et al. A light-triggered self-reinforced nanoagent for targeted chemo-photodynamic therapy of breast cancer bone metastases *via* ER stress and mitochondria mediated apoptotic pathways. *J Control Release* 2020;**319**:119–34.
32. Au KM, Satterlee A, Min Y, Tian X, Kim YS, Caster JM, et al. Folate-targeted pH-responsive calcium zoledronate nanoscale metal-organic frameworks: turning a bone antiresorptive agent into an anticancer therapeutic. *Biomaterials* 2016;**82**:178–93.
33. Chu W, Huang Y, Yang C, Liao Y, Zhang X, Yan M, et al. Calcium phosphate nanoparticles functionalized with alendronate-conjugated polyethylene glycol (PEG) for the treatment of bone metastasis. *Int J Pharm (Amst)* 2017;**516**:352–63.
34. Zhao L, Wientjes MG, Au JL. Evaluation of combination chemotherapy: integration of nonlinear regression, curve shift, isobologram, and combination index analyses. *Clin Canc Res* 2004;**10**:7994–8004.
35. Mei D, Chen B, He B, Liu H, Lin Z, Lin J, et al. Actively priming autophagic cell death with novel transferrin receptor-targeted nanomedicine for synergistic chemotherapy against breast cancer. *Acta Pharm Sin B* 2019;**9**:1061–77.
36. He X, Andersson G, Lindgren U, Li Y. Resveratrol prevents RANKL-induced osteoclast differentiation of murine osteoclast progenitor RAW 264.7 cells through inhibition of ROS production. *Biochem Bioph Res* 2010;**401**:356–62.
37. Vincent C, Kogawa M, Findlay DM, Atkins GJ. The generation of osteoclasts from RAW 264.7 precursors in defined, serum-free conditions. *J Bone Miner Metabol* 2009;**27**:114–9.
38. Kim JH, Kim EY, Lee B, Min JH, Song DU, Lim JM, et al. The effects of Lycii Radicis Cortex on RANKL-induced osteoclast differentiation and activation in RAW 264.7 cells. *Int J Mol Med* 2016;**37**:649–58.
39. Wang F, Chen L, Zhang R, Chen Z, Zhu L. RGD peptide conjugated liposomal drug delivery system for enhance therapeutic efficacy in treating bone metastasis from prostate cancer. *J Control Release* 2014;**196**:222–33.
40. Zhou F, Mei J, Han X, Li H, Yang S, Wang M, et al. Kinsenoside attenuates osteoarthritis by repolarizing macrophages through inactivating NF-κB/MAPK signaling and protecting chondrocytes. *Acta Pharm Sin B* 2019;**9**:973–85.
41. Glausch A, Loeffler R, Sigg J, inventors. Pharmaceutical products comprising bisphosphonates. United States Patent US7932241B2. 2003 September 18.
42. Silver I, Murrills R, Etherington D. Microelectrode studies on the acid microenvironment beneath adherent macrophages and osteoclasts. *Exp Cell Res* 1988;**175**:266–76.
43. Clarke B. Normal bone anatomy and physiology. *Clin J Am Soc Nephrol* 2008;**3**:S131–9.
44. Swami A, Reagan MR, Basto P, Mishima Y, Kamaly N, Glavey S, et al. Engineered nanomedicine for myeloma and bone microenvironment targeting. *P Natl A Sci India B* 2014;**111**:10287–92.
45. Kelland L. The resurgence of platinum-based cancer chemotherapy. *Nat Rev Canc* 2007;**7**:573–84.
46. Räikkönen J, Crockett JC, Rogers MJ, Mönkkönen H, Auriola S, Mönkkönen J. Zoledronic acid induces formation of a pro-apoptotic ATP analogue and isopentenyl pyrophosphate in osteoclasts *in vivo* and in MCF-7 cells *in vitro*. *Br J Pharmacol* 2009;**157**:427–35.
47. Ibrahim T, Liverani C, Mercatali L, Sacanna E, Zanoni M, Fabbri F, et al. Cisplatin in combination with zoledronic acid: a synergistic effect in triple-negative breast cancer cell lines. Corrigendum in/10.3892/ijo. 2016.3613. *Int J Oncol* 2013;**42**:1263–70.
48. Fujise K, Zhang D, Liu Jl, Yeh ET. Regulation of apoptosis and cell cycle progression by MCL1 differential role of proliferating cell nuclear antigen. *J Biol Chem* 2000;**275**:39458–65.
49. Ellard SL, Clemons M, Gelmon KA, Norris B, Kennecke H, Chia S, et al. Randomized phase II study comparing two schedules of everolimus in patients with recurrent/metastatic breast cancer: NCIC clinical trials group IND. 163. *J Clin Oncol* 2009;**27**:4536–41.
50. Lehmann BD, Bauer JA, Chen X, Sanders ME, Chakravarthy AB, Shyr Y, et al. Identification of human triple-negative breast cancer subtypes and preclinical models for selection of targeted therapies. *J Clin Invest* 2011;**121**:2750–67.
51. Moriceau G, Ory B, Mitrofan L, Riganti C, Blanchard F, Brion R, et al. Zoledronic acid potentiates mTOR inhibition and abolishes the resistance of osteosarcoma cells to RAD001 (Everolimus): pivotal role of the prenylation process. *Cancer Res* 2010;**70**:10329–39.

52. Meng F, Wang J, Ping Q, Yeo Y. Quantitative assessment of nanoparticle biodistribution by fluorescence imaging, revisited. *ACS Nano* 2018;**12**:6458−68.
53. Shalgunov V, Zaytseva-Zotova D, Zintchenko A, Levada T, Shilov Y, Andreyev D, et al. Comprehensive study of the drug delivery properties of poly (L-lactide)-poly (ethylene glycol) nanoparticles in rats and tumor-bearing mice. *J Control Release* 2017;**261**:31−42.
54. Swami A, Reagan MR, Basto P, Mishima Y, Kamaly N, Glavey S, et al. Engineered nanomedicine for myeloma and bone microenvironment targeting. *Proc Natl Acad Sci U S A* 2014;**111**:10287−92.
55. Valkenburg KC, Steensma MR, Williams BO, Zhong Z. Skeletal metastasis: treatments, mouse models, and the Wnt signaling. *Chin J Canc* 2013;**32**:380−96.
56. Yerushalmi R, Woods R, Ravdin PM, Hayes MM, Gelmon KA. Ki67 in breast cancer: prognostic and predictive potential. *Lancet Oncol* 2010;**11**:174−83.
57. Sun W, Ge K, Jin Y, Han Y, Zhang H, Zhou G, et al. Bone-targeted nanoplatform combining zoledronate and photothermal therapy to treat breast cancer bone metastasis. *ACS Nano* 2019;**13**:7556−67.
58. Li D, Nie W, Chen L, McCoul D, Liu D, Zhang X, et al. Self-assembled hydroxyapatite-graphene scaffold for photothermal cancer therapy and bone regeneration. *J Biomed Nanotechnol* 2018;**14**:2003−17.
59. Son HS, Lee J, Lee HI, Kim N, Jo YJ, Lee GR, et al. Benzydamine inhibits osteoclast differentiation and bone resorption *via* down-regulation of interleukin-1β expression. *Acta Pharm Sin B* 2020;**10**:462−74.